GEOMECHANICAL ANALYSIS OF ROCK BRITTLENESS WITH COMPARISONS TO THE MINERALOGICAL BRITTLENESS INDEX

by

DEREK THOMAS BAMMEL

Presented to the Faculty of the Graduate School of

The University of Texas at Arlington in Partial Fulfillment

of the Requirements

for the Degree of

MASTER OF SCIENCE IN GEOLOGY

THE UNIVERSITY OF TEXAS AT ARLINGTON

May 2016

Supervising Committee:

Dr. John Wickham, Supervising Professor
Dr. Ashley Griffith
Dr. Xinbao Yu
Dr. Qinhong Hu

Acknowledgements

I would like to express my sincerest gratitude to all of the individuals who provided me with support and who made it possible for me to reach my academics goals while at the University of Texas at Arlington. I would first like to thank Dr. John S. Wickham for his patience, ongoing support, and overall mentorship. He has provided me with not only the critical thinking ability I have today, but the tools needed to further my career. I would like to give a special thanks to my thesis committee. To Dr. Ashley Griffith, thank you for providing me additional mentorship throughout the graduate program as well as asking the necessary questions to broaden my knowledgebase. To Dr. Xinbao Yu, my appreciation goes out to you for allowing me access to your laboratory as well as providing assistance from your PhD candidates. I would also like to thank my friends and family for their mental and emotional support throughout the graduate program. Thank you to my father, Ronald Bammel, and my mother, Cynthia Bammel, for your ongoing support, guidance, and advice. A special thank you goes out to my friends Matthieu and Tabatha Chansard for their additional guidance throughout the past year. Finally, I would like to express my deepest gratitude to my girlfriend Megan. Without her unwavering support, none of this would be possible.

April 18th, 2016

Abstract

GEOMECHANICAL ANALYSIS OF ROCK BRITTLENESS WITH COMPARISONS TO THE MINERALOGICAL BRITTLENESS INDEX

Derek Thomas Bammel, MS

The University of Texas at Arlington, 2016

Supervising Professor: John S. Wickham

A significant area of research within the Oil and Gas industry centers around the understanding of rock brittleness and fracture mechanics related to inducing and extending hydraulic fractures. This study defines rock brittleness as the fracture density, or the fracture surface area per unit volume (m^{-1}), at a particular strain state.

The first goal of this research was to test whether or not the strain conditions of various rock layers were constant using a geomechanically derived equation,

$$\frac{F_d K_{Ic}^2}{4\mu^2(1+\nu)} = A\frac{\nu}{1-2\nu} + B,$$

where F_d is fracture density, K_{ic} is fracture toughness, μ is the shear modulus, ν is Poisson's Ratio, and A and B are functions of the strain invariants. If the strain states were similar, the results would plot as a straight line with a positive slope. Analysis of the collected samples consisted of acoustic testing for P and S-wave velocities as well as mercury intrusion porosimetry for density and porosity. Fracture density measurements and samples were taking at three separate locations: Palo Duro Canyon, TX, Bighorn Basin, WY, and along Highway 90 in Del Rio, TX.

The second goal was to compare the geomechanical definition of brittleness with a mineralogical brittleness definition commonly used in the industry. The mineralogical content of each sample was estimated using X-Ray Diffraction and then used to calculate

the Brittleness Index (Wang and Gale, 2009) which was compared with the Geomechanical Brittleness. Since the geomechanical brittleness equation is based on fracture mechanics, the mineralogical brittleness should correlate with the geomechanical brittleness. If it doesn't the mineralogical brittleness should be modified or discarded.

Using the Geomechanical Brittleness equation, the data from Palo Duro, TX produced a positive correlation of 0.9701, indicating that the strain was constant through each layer. It was determined that a correlation can't be definitively established for samples from Bighorn Basin, WY due to limited sampling. Finally, a poor correlation coefficient of 0.005 from the Highway 90 Road Cuts in Del Rio, TX indicates that the samples from were either subjected to different strain states or deformed beyond their tensile strength. The results for the geomechanical brittleness and mineralogical brittleness comparisons show that there is a strong positive correlation of 0.99 for the Palo Duro Canyon, TX samples. The results for Bighorn Basin, WY and Del Rio, TX suggest that the geomechanical brittleness does not correlate with the mineralogical brittleness, both yielding a low correlation coefficient.

Because of the inconclusive correlation for two of the study locations, additional analysis is recommended for the samples from Del Rio, TX and Bighorn Basin, WY.

Table of Contents

List of Illustrations

List of Tables

Chapter 1

Introduction

The efficiency of hydrocarbon production, particularly in tight reservoirs, is typically controlled by variables related to fracture density/intensity. Due to a strong correlation between greater hydrocarbon recoveries and high fracture density, it is important to understand the effectiveness of induced fracture density in tight reservoirs. Rock brittleness, defined as the fracture density at a particular strain state, is a significant variable that controls hydraulic fracturing during completions. Theoretical formulations indicate that fracture density can be predicted by strain energy and rock properties. Notable studies on the relationship of strain energy to fracture density include Blanton (1981), Chong et al (1980), and Singh (1989). Mode I fracture spacing is defined as the average perpendicular distance between joints of a single joint set in an outcrop, with units of L. Berg (2012) refers to fracture density as the inverse of fracture spacing. Because joint spacing can be measured relatively easily, its inverse is used to estimate fracture density, which cannot be easily measured. Fracture spacing and density can be influenced by numerous variables, including stress shadows and fracture interaction (Wong et al., 2013 and Nagel, 2013), particularly when the ultimate strength of the rock layer is exceeded and the layer is saturated with fractures. Other studies of fracture spacing and fracture density include (Barthelemy, 2009 Guiton and Daniel, 2009; Kimiagar, 2012; Smith, 2012; Ferrill, 2014). Within the petroleum industry, brittleness is commonly measured using mineral percentages utilizing the Brittleness Index derived from XRD, XRF, and various well logs. Both Jarvie et al. (2007) and Wang and Gale (2009) proposed equations to determine brittleness via mineralogical composition, known as the Brittleness Index. Jarvie et al. (2007) defines brittleness as the weight percent of quartz (Qz), Carbonate, and clay (Cl) using Eq. 1

$$Brittlenes\ Index\ (BI) = \frac{Qz}{Qz + Carbonate + Cl} \quad \text{Eq.1}$$

The Wang and Gale (2009) Use the weight percent of quartz and clay but include the weight percent Dolomite (Dol), Limestone, and Total Organic Carbon (TOC) using Eq 2

$$BI = \frac{Qz + Dol}{Qz + Dol + Limestone + Cl + TOC} \quad \text{Eq. 2}$$

Higher indices indicate greater brittleness while lower indices indicate less brittle rock. Some studies, such as Altamar and Marfurt (2014), indicate that the results from the two differing procedures correlate well in certain cases, particularly in quartz-rich rock.

The purpose of this study is to use a geomechanical equation (Equation 13), to predict fracture density under constant strain conditions. Brittleness is defined here as fracture density at a particular strain state. Of two rocks at the same strain state, the one with the greater fracture density is more brittle. The fracture density/brittleness results will be compared with the mineralogical Brittleness Index, both calculated from the same specimen.

Three separate study locations were chosen for this project: Palo Duro Canyon, TX, Bighorn Basin, WY, and Highway 90 West of Del Rio, TX. Brittleness predicted by the geomechanical equation will be compared to the mineralogical brittleness index using samples and measurements from these localities.

Chapter 2

Geomechanical Brittleness: Theory and Derivation

Fracture density is fracture surface area/volume with units of $(length)^{-1}$ (Wickham et al 2013). Below is a table of the symbols used throughout this paper:

Symbol	Definition
U	Energy
U_v	Strain energy in volume v
V	Volume
A	Area
G	Energy release rate
σ	Stress
ε	Strain
F_d	Fracture Density
U_a	Energy per fracture area created
μ	Elastic Shear Modulus
v	Poisson's Ratio
E	Young's Modulus
ρ	Mass Density
V_p	Compressional Wave Velocity
V_s	Shear Wave Velocity
I_1	First Strain Invariant
I_2	Second Strain Invariant
K_{IC}, K_{IIC}, K_{IIIC}	Critical Stress intensity factors for mode I, II, and III fractures

The equation we use to relate fracture density to strain energy density was proposed by Sih (1985), and is shown in Eq. 3

$$\left(\frac{dA}{dV}\right)_i \left(\frac{dU}{dA}\right)_i = \left(\frac{dU}{dV}\right) \quad \text{Eq. 3}$$

A is the fracture surface area, ***V*** is volume, and ***U*** is the strain energy. Integrating the above equation over a volume element yields a more useful form

$$(F_d)(U_a) = U_v \qquad \text{Eq. 4}$$

$\boldsymbol{F_d}$ is the fracture surface area in the volume of interest (fracture density), $\boldsymbol{U_a}$ is the energy per fracture area created or fracture surface energy, and $\boldsymbol{U_v}$ is the strain energy in the volume of interest (strain energy density). As stated in Wickham et al (2013),

"$\boldsymbol{U_a}$ in this formulation is not just fracture surface energy, but all the energy that goes into producing new surface area associated with a fracture: new fracture surface energy, energy dissipated as heat, acoustic emissions and other crack growth in the process zone. $\boldsymbol{U_a}$ takes into account the energy associated with damage and plastic deformation emphasized by Busetti et al. (2012). $\boldsymbol{U_v}$ is understood to be the strain energy associated with a volume. Below the elastic yield point $\boldsymbol{U_v}$ might be associated with closing cracks and a reduction of fracture density. Above the yield point $\boldsymbol{U_v}$ would be associated with increasing volume, fracture density and plastic deformation. Above the yield point, we assume that the matrix material away from the fracture and damage zones continues to behave elastically building elastic strain energy; however some of that elastic energy, $\boldsymbol{U_v}$, is converted into fracture energy. In this energy approach, it should not matter whether the material yields in tension or compression. The important result of this theory is that fracture density measured over some volume of rock is a function of the strain energy in that same volume of rock at the time the fractures formed."

Strain energy density in Eq. 5 is generally expressed as

$$\boldsymbol{U_v} = \frac{1}{2}\left(\sigma_{xx}\epsilon_{xx} + \sigma_{yy}\epsilon_{yy} + \sigma_{zz}\epsilon_{zz}\right) + \left(\sigma_{xy}\epsilon_{xy} + \sigma_{yz}\epsilon_{yz} + \sigma_{xz}\epsilon_{xz}\right) \qquad \text{Eq. 5}$$

Assuming linear elasticity, the strain energy in a rock volume of constant elastic properties yields

$$\boldsymbol{U_v} = \frac{\nu\mu}{1-2\nu}\left(\epsilon_{xx} + \epsilon_{yy} + \epsilon_{zz}\right)^2 + \mu\left(\epsilon^2{}_{xx} + \epsilon^2{}_{yy} + \epsilon^2{}_{zz}\right) + 2\mu\left(\epsilon^2{}_{xy} + \epsilon^2{}_{yz} + \epsilon^2{}_{xz}\right) \qquad \text{Eq. 6}$$

U_v is the total elastic strain energy available to create fracture surface area; v is poisson's ratio and μ is the shear modulus. Eq. 6 can be written in terms of the strain invariants:

$$U_v = \mu(A\frac{v}{1-2v} + B) \qquad \text{Eq. 7}$$

Both A and B are constants expressed in terms of the strain invariants, I_1 and I_2, where,

$$I_1 = (\epsilon_{xx} + \epsilon_{yy} + \epsilon_{zz})$$

$$I_2 = (\epsilon_{xx}\epsilon_{yy} + \epsilon_{yy}\epsilon_{zz} + \epsilon_{zz}\epsilon_{xx})$$

$$A = I_1^2 = \epsilon_x{}^2 + \epsilon_y{}^2 + \epsilon_z{}^2 + 2(\epsilon_{xx}\epsilon_{yy} + \epsilon_{yy}\epsilon_{zz} + \epsilon_{zz}\epsilon_{xx})$$

$$B = I_1^2 - 2I_2 = \epsilon_x{}^2 + \epsilon_y{}^2 + \epsilon_z{}^2$$

Substituting Eq. 7 into Eq. 4 yields

$$F_d = \frac{\mu}{U_a}(A\frac{v}{1-2v} + B) \qquad \text{Eq. 8}$$

Fracture surface energy, U_a, is related to the critical energy release rate, G_c. Fracture propagation occurs as the energy release rate, G_c, reaches the critical value. For brittle elastic materials, the following equation can be derived (Backers, 2005)

$$G_c = 2U_a \qquad \text{Eq. 9}$$

Irwin (1958) showed the equivalence of energy release rate and the stress intensity factor, ***K***. Each of the three modes of fracturing consists of an associated stress intensity factor. According to Irwin (1958) $\boldsymbol{G_c}$ is related to the stress intensity factors by

$$\boldsymbol{G_c} = \frac{\boldsymbol{K_{Ic}^2}}{\boldsymbol{2\mu(1+\nu)}} + \frac{\boldsymbol{K_{IIc}^2}}{\boldsymbol{2\mu(1+\nu)}} + \frac{\boldsymbol{K_{IIIc}^2}}{\boldsymbol{2\mu}} \quad \text{Eq. 10}$$

Because the focus of this study is on Mode I fractures, Eq. 10 can be simplified to

$$\boldsymbol{G_c} = \frac{K_{Ic}^2}{2\mu(1+\nu)} \quad \text{Eq. 11}$$

By combining Eqs. 9 and 11, the relationship for $\boldsymbol{U_a}$ becomes

$$\boldsymbol{U_a} = \frac{K_{Ic}^2}{4\mu(1+\nu)} \quad \text{Eq. 12}$$

Substituting Eq. 12 into Eq. 8 produces the geomechanical equation predicting fracture density and brittleness

$$\boldsymbol{F_d} = \frac{4\mu^2(1+\nu)}{K^2{}_{Ic}}\left(A\frac{\nu}{1-2\nu} + B\right) \quad \text{Eq. 13}$$

Eq. 13 can be rearranged into a dimensionless linear form if the strain state ***A*** and ***B*** is constant (Wickham et al, 2013)

$$\frac{F_d K_{Ic}^2}{4\mu^2(1+\nu)} = A\frac{\nu}{1-2\nu} + B \quad \text{Eq. 14}$$

2.1 Mechanics of Jointing and Rock Failure

The classification of fractures is based on the rock displacement relative to the fracture surface (Figure 2-1).

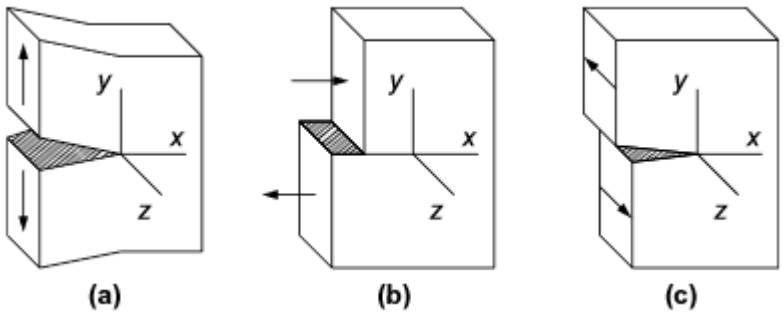

Figure 2-1. Basic fracture modes: (a) Mode I - opening, (b) Mode II - sliding, (c) Mode III tearing (Sun and Jin, 2012).

The focus of this study is exclusively on mode I fractures, which can be defined as open planes parallel to the maximum compressive stress, or σ_1, and perpendicular to the least principal stress, σ_3. According to Bourne and Willemse (2001), these fractures form because the rock cannot sustain the in-situ least effective stress. The Coulomb-Mohr criterion is often used to estimate shear failure in brittle rock by plotting the shear stress versus the normal stress. Since our focus is on mode I fractures, the Coulomb-Mohr failure criterion does not apply.

The mechanics of linear elasticity predicts that the orientation of mode I fractures are generally controlled by the remote stress field at the time of fracture propagation. The crack growth within a brittle rock is governed by the stress field around the crack tip along with the rock toughness (Jin and Sun, 2005). When plasticity develops but remains well contained to the crack tip region, this is referred to as Small Scale Yielding (Thomas et al, 2014). Small Scale Yielding (SSY) implies that when a small load is applied to material with a pre-existing fracture, the stress near the crack tip is magnified leading to SSY and crack propagation. Stress shadows and tensile failure are concepts that are associated with SSY, crack propagation and mode I fracture density.

Commonly referred to as the stress field change, stress shadows (Figure 2-2) have been described by Nagel et al (2013) as "the increase in the minimum horizontal (compressive) stress, Shmin, caused by a hydraulic fracture". Others such as Nagel & Sanchez-Nagel (2011) note that the increase in the least principal stress (stress shadow) can extend large distances around a fracture. Touching stress shadows means that fractures can no longer develop within that region but existing fractures can propagate until the layer boundary is met which means that the layer has failed. Equations 13 and 14 generally apply before the stress shadows touch and before the joints propagate throughout the entire layer.

While tensile failure is an important concept in regards to SSY, the tensile strength of rock is relatively small when compared to the compressional strength (Zoback, 2010). Tensile failure is important when pore pressures are high inducing effective tensile stress at depth, which is what happens around a wellbore during hydraulic fracturing. Zoback (2015) states that high pore pressure can also occur naturally generating mode I joints in rock. He goes on to point out that the extension of these tensile fractures also occurs during hydraulic fracturing operations when fluid

pressure is raised above the *in-situ* least principal stress, further propagating the pre-existing fractures. These fractures are of course filled with a proppant such as sand or another material to increase formation permeability.

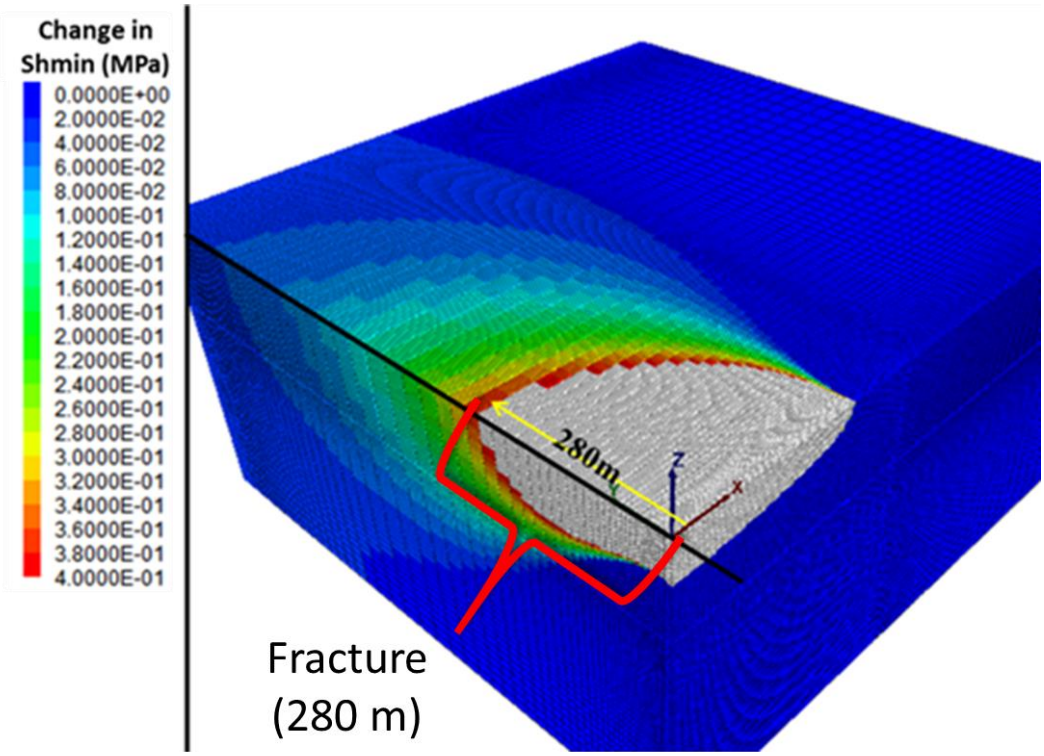

Figure 2-2. Stress shadow contours from a single 280-meter-long hydraulic fracture in the y-z plane. Modified from Nagel et al (2013)

Chapter 3

Geological Setting

3.1 Location 1: Palo Duro Canyon, Texas.

Within Palo Duro Canyon, located along the northern edge of Palo Duro Basin, fracture density measurements were taken on two of the exposed formations: The Dewey Lake/Quartermaster Formation (upper Permian) and the Trujillo Formation (Triassic). Palo Duro Basin is a shallow asymmetric intracratonic basin primarily filled with Mississippian, Pennsylvanian, and Permian age strata. Structurally, the basin is surrounded by fault-bounded uplifts that were active and ultimately exposed during the Pennsylvanian (Rose, 1969). The Amarillo Uplift, a granitic and gabbroic mixture of Precambrian and Cambrian block, separates the Palo Duro and Anadarko Basins. Along the southern margin of Palo Duro Basin, the Matador Arch, consisting of block-faulted basement rocks, separates the Palo Duro and Midland Basins (Handford and Dutton, 1980). The western rim is bordered by the Bravo Dome and Sierra Grande uplift, while the eastern border is a north-south trending basement high, separating the Palo Duro Basin from the Hardeman Basin (Handford and Dutton, 1980).

The Palo Duro Basin was formed by compressional events during the Pennsylvanian that supplied large amounts of arkosic sediment to the surrounding area (Rose, 1986). Most of the deformation with the region occurred throughout the Pennsylvanian, with subdued events continuing through the Permian (Presley, 1987). The upper Permian consists of evaporate-red bed sequences occurring in restricted, back-shelf sabkha environments (Dutton et al., 1978). These thin siltstone beds make up what is now the Dewey Lake/Quartermaster Formation. Basin development ceased after the Permian, ending marine deposition within the Panhandle area of Texas. The Trujillo

Formation is believed to represent deposition in high-constructive lobate delta, meanderbelt and valley-fill systems (Murry, 1989).

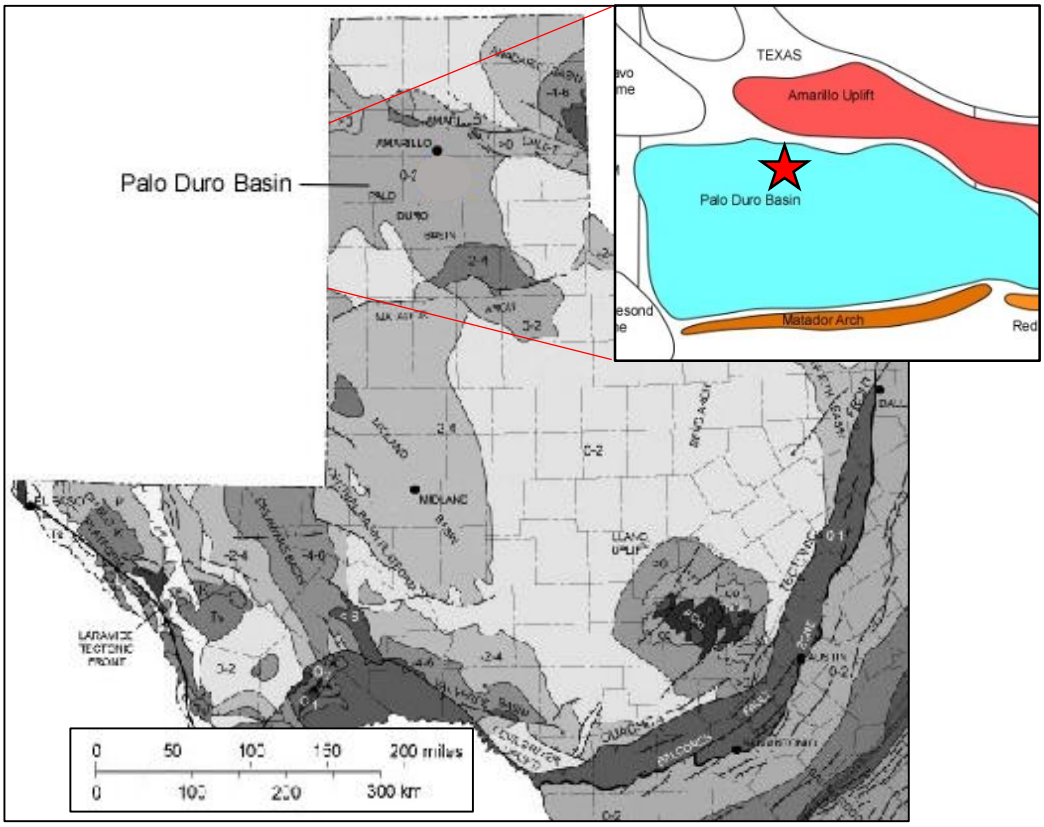

Figure 3-1. Tectonic Map of Texas showing the location of Palo Duro Basin, TX. Red star denotes Location 1 (Palo Duro Canyon, TX). Modified from the Tectonic Map of Texas, 1997

3.2 Location 2: Bighorn Basin, Wyoming

Fracture Density measurements and samples were collected from the top of the Bighorn Dolomite (Ordovician) along the eastern rim of Bighorn Basin, as seen in figure 3. Located between the Bighorn Mountains and the Absaroka Range, Wyoming, the Bighorn Basin is a Laramide, northwest-southeast trending foreland basin. The basin itself is an asymmetric syncline with thrust and antithetic faults bounding both sides. The northeast, eastern, and southern boundaries of the basin are formed by basement-cored uplifts, which are flanked by highly folded and faulted sedimentary rocks (Finn et al., 2010). Sheep Mountain is a doubly plunging, asymmetric anticline oriented parallel to the eastern Bighorn Basin margin, striking N40°W (Simmons and Scholle, 1990). Due to the 600 to 700-foot uplift of Sheep Mountain, the Bighorn Dolomite is exposed along small river cuts northeast of Sheep Mountain. As noted in Simmons and Scholle (1990), a subtle angular unconformity within the Madison Group near Sheep Canyon implies that some pre-Laramide deformation and uplift of the Sheep Mountain area occurred during Mississippian time, ultimately effecting older formations below.

Throughout most of this its history, the Bighorn Basin area was in the Western Interior Seaway forming from foreland basin subsidence and eustatic sea-level rise (Steidtmann, 1993). Most of the Paleozoic and lower Mesozoic rocks originated as sediment deposited in shallow seas, covering the western continental shelves (Fox and Dolton, 1996).

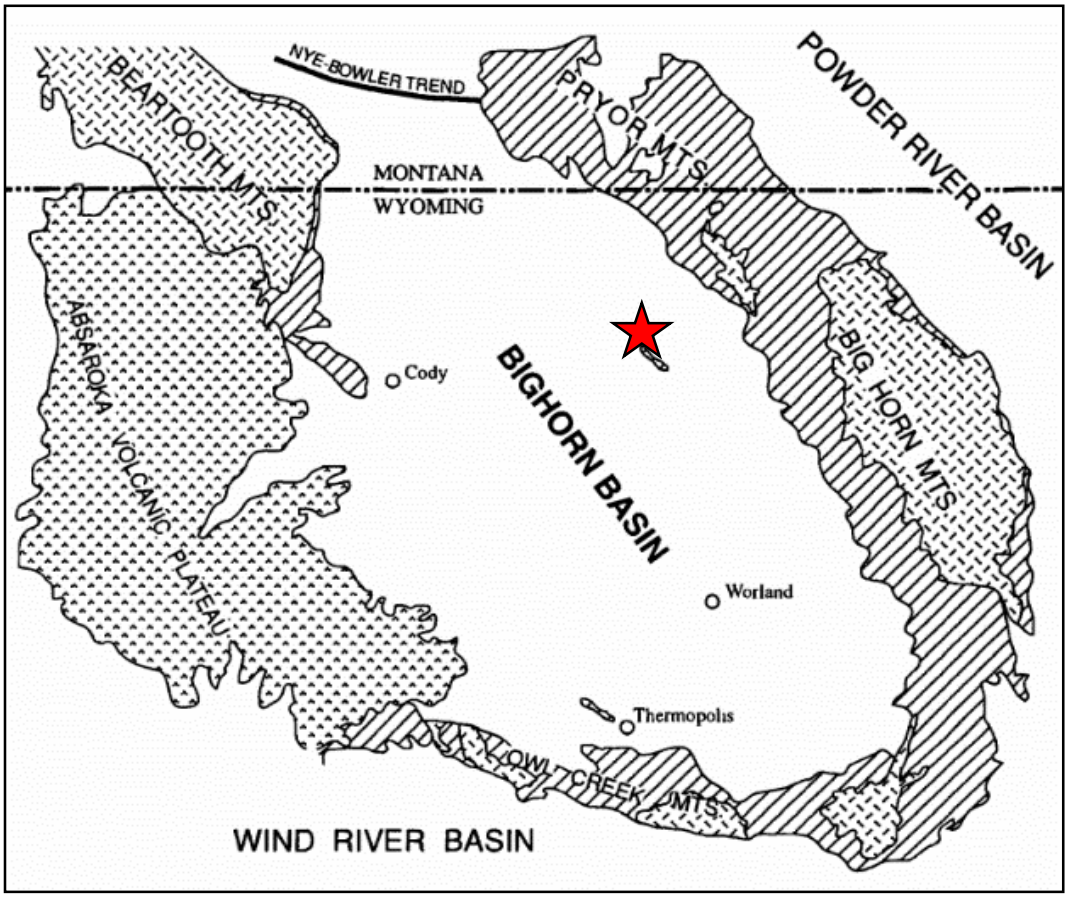

Figure 3-2. Map of Bighorn Basin with surrounding rock groups. The red star denotes the location of study area two. Modified from Fox and Dolton (1996)

3.3 Location 3: Highway 90 Road Cuts, Val Verde County, TX.

Along US 90, between Del Rio and Langtry, Texas, numerous roadcuts display well-preserved exposures of Lower and Upper Cretaceous rocks. Measurements of fracture density and rock samples were taken from five exposed formations along US Highway 90: Salmon Peak (Lower Cretaceous), Del Rio Formation (Upper Cretaceous), Buda Limestone (Upper Cretaceous), Boquillas/Eagle Ford Formation (Upper Cretaceous), and Atco Chalk (Upper Cretaceous).

As shown in Figure 3-3, the structural environment of Location 3 consists of the Central Basin Platform (separated by the Sheffield Channel), Ozona Arch, and Eastern Shelf. The Ozona Arch and Eastern Shelf are intra-foreland uplifts along the northern margin of Val Verde Basin (Hamlin, 2009). To the south, Ouachita rocks were thrust over North American basement rocks, forming a synorogenic convergent margin during the Late Pennsylvanian (Hamlin, 2009). Sediment was provided by the northern margin intra-foreland uplifts while the Ouachita thrust belt supplied sediment from the south (Hamlin, 2009). During plate convergence, the aforementioned uplifts were briefly exposed, supplying sediment to the surrounding area (Hamlin, 2009). During the Cretaceous, after the Late Paleozoic orogeny, the continental margin in the Texas area subsided, allowing the sea to gradually progress further inland, producing thick, calcareous shelf sediment. Initially deposited as a pelagic lime mudstone in the Early Cretaceous, most of the Salmon Peak Formation formed in a low energy, open embayment (Clarke, 2003). Due to the intercontinental seaway connection, hundreds of feet of Upper Cretaceous marine limestone, chalk, and mudstone accumulated in the South Texas area (Ward, 2006). Among these formations are the Del Rio Formation, Buda Limestone and the Boquillas/Eagle Ford Formation. Approximately 200 feet of the Boquillas/Eagle Ford Formation was deposited during the Cenomanian-Turonian Oceanic

Anoxic event (Lock et al., 2010). Finally, the Atco Chalk, produced by shallow-marine deposition, marks the top of the Cretaceous in the Val Verde Basin area (Pearson, 2012).

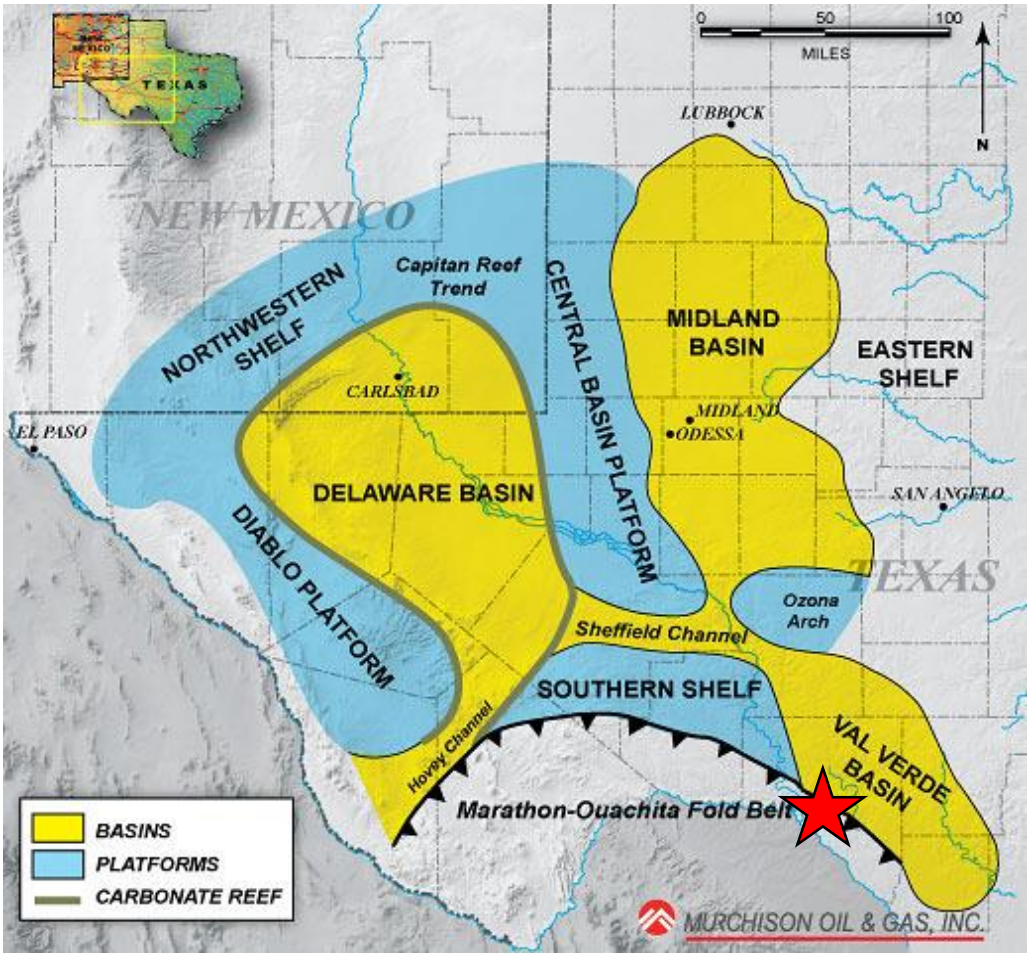

Figure 3-3. Index map showing the location of the Marathon Thrust Belt relative to the Permian foreland basins. Red star designates location 3. Modified from Hickman et al. (2009)

Chapter 4

Methods and Procedures

Utilizing the scanline sampling method, fracture densities were calculated at largely varying locales. These measurements were taken from numerous beds, preferably within close proximity of one another. After fracture density was measured, samples from each station were collected and brought back to the UTA labs where acoustic properties were measured. Using mercury intrusion porosimetry, samples were then analyzed for each station in order to measure density and porosity. Finally, X-Ray Diffraction was used to extract mineral percentages for additional analysis.

4.1 Field Measurements

The fracture density measurement method used in this research is scanline sampling as described by Zeeb et al. (2013). Data is collected from the fracture/joint sets that intersect a scanline. According to Chiles et al. (2008), this method entails measuring: (1) distances to fractures along scanlines on representative areas of a layer; (2) the fracture length of each fracture along the scanlines in the area; (3) fracture orientation; (4) thickness of the layer; (5) orientation of the layer; (6) orientation of the representative area containing the scanline; and (7) orientation of the scanlines. Using a tape measure as the scanline, the length or distance of each fracture along the scanline was recorded, along with fracture length, fracture orientation, bed thickness and orientation.

Scanline sampling can produce a bias that has to be corrected. If the fractures are not perpendicular to the scanline, they are undersampled. Each fracture crossing the

scanline is given a weighting factor based on their angular relationship to the scanline in order to calculate their true fracture density (Figure 4-1).

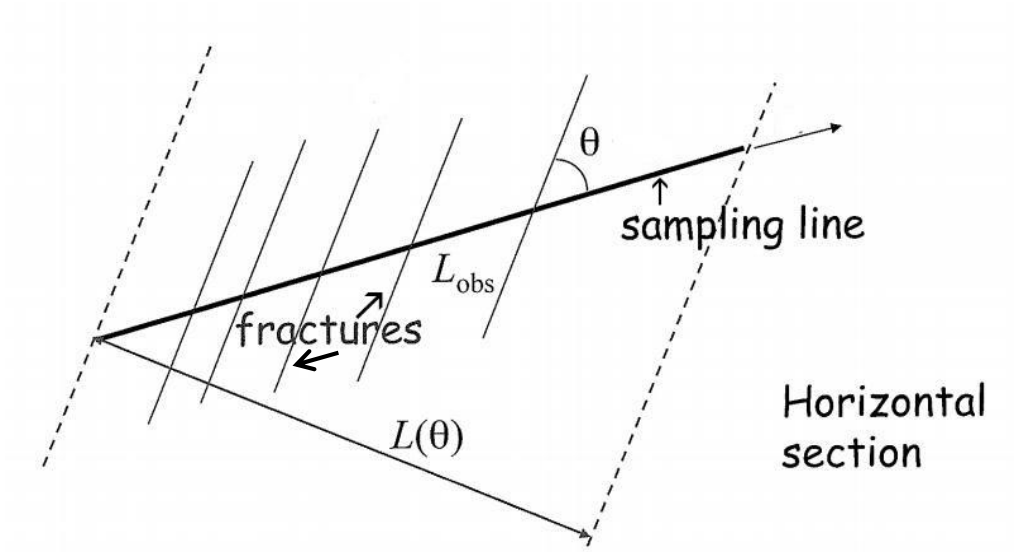

Figure 4-1. Fracture density correction based on fracture angle in relation to the scanline, see text for description (Chiles et al. 2008)

Five fractures are shown along the scanline L_{obs} in Figure 4-1. To get their true fracture density, divide the number of fractures (5) by the length perpendicular to them, L(θ). With the knowledge that

$$L(\theta) = L_{obs} * \sin(\theta)$$

We can equate the above equation to

$$\frac{[f1 + f2 + f3 + f4 + f5]}{L_{obs} * \sin(\theta)}$$

This is equivalent to

$$\frac{\left[\frac{f1}{\sin(\theta)} + \frac{f2}{\sin(\theta)} + \frac{f3}{\sin(\theta)} + \frac{f4}{\sin(\theta)} + \frac{f5}{\sin(\theta)}\right]}{L_{obs}}$$

Where

$$\frac{f(n)}{\sin(\theta)} = \frac{1}{\sin(\theta)}$$

The above equation assumes that each fracture has the exact same orientation. If each of the measured fractures have a different orientation, then each weighting factor would be different:

$$\frac{\left[\frac{f1}{\sin(\theta_1)} + \frac{f2}{\sin(\theta_2)} + \frac{f3}{\sin(\theta_3)} + \frac{f4}{\sin(\theta_4)} + \frac{f5}{\sin(\theta_5)}\right]}{L_{obs}}$$

When θ = 90°, the scanline reads correctly, meaning the weighting factor is equivalent to 1. With that said, if θ = 60°, then the weighting factor is

$$\frac{1}{\sin(60)} = 1.154$$

Those fractures are underrepresented on the scanline L_{obs} and need a larger weighting factor. Fractures perpendicular to the scanline are given a value of one while non-perpendicular fractures produce a value greater than one. If more than one scanline is used per station, weighting factors are added for all the scanlines and divided by the combined length of the scanlines.

Considering that most of the outcrops are in road cuts, there are fractures due to blasting. Generally, these induced fractures are easily spotted parallel or adjacent to visible boreholes. Only mode I regional joint sets were measured, which could be distinguished from blasting fractures. Rose diagrams, generated by Dr. Rick Allmendinger's Stereonet 9 software, were added to verify the primary fracture orientations for each locality.

4.1.1 Palo Duro Canyon, TX

Due to the difficulty in reaching most exposed outcrop within the canyon, fracture density data was only collected from three stations. The first station, PD STA-1, measured the Quartermaster Formation at the base of the canyon. The other two stations, PD STA-2 and PD STA-3 were measured in the Trujillo Formation (Figure 4-2). Five scanlines were used to acquire the fracture density for PD STA-1, each with varying trends (Table 2). Using the weighting method shown above, the fracture density for PD STA 1 was 0.512 m^{-1} (Table 2) with strike orientations favoring the NW and NE directions (Figure 4-3). Two scanlines were used for PD STA-2, which showed a fracture density of 0.843 m^{-1} (Table 3). Only one scanline was used for PD STA-3, resulting in a fracture density of 1.339 m^{-1} (Table 4). Both PD STA-2 and PD STA-3 also favored NW and NE strike orientations, shown in Figure 4-4. Although measurements from PD STA-2 and 3 were taken from the same formation, their mechanical properties differed resulting in different fracture densities.

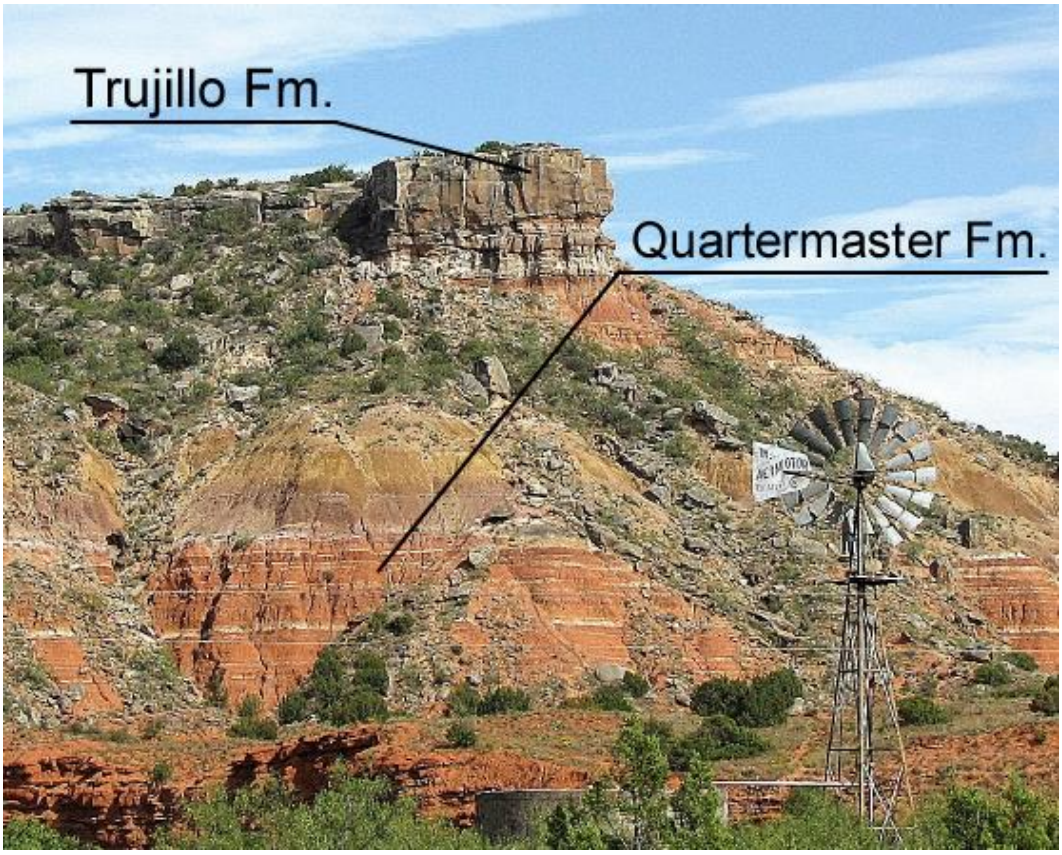

Figure 4-2. Measured formations within Palo Duro Canyon, TX

Table 4-1. Quartermaster Formation Data – Station 1 - PD STA-1

Station	UTM Coordinates	Strike of Outcrop (Right Hand Rule)	Dip of Outcrop (Right Hand Rule)	Thickness of Bed (M)	Strike of Bed (Right Hand Rule)	Dip of Bed (Right Hand Rule)	Trend of Scanline	Plunge of scanline	Length of Scanline (M)	Scanline Vector x = North	Scanline Vector y = East	Scanline Vector z = down	Sample #
Palo Duro 1 (PD STA 1)	14S 254932 E 3874149 N +/- 4 meters		Horizontal	.15 to .381		Horizontal	172	0	9.75	-0.99	0.14	0.00	PD STA-1
						Scanline 1	172	0	9.75	-0.99	0.14	0.00	
						Scanline 2	342	0	10	0.95	-0.31	0.00	
						Scanline 3	255	0	9.144	-0.26	-0.97	0.00	
						Scanline 4	273	0	3.96	0.05	-1.00	0.00	
						Scanline 5	265	0	1.21	-0.09	-1.00	0.00	

Scan Line #	Trend	Fracture Distance (ft)	Fracture Distance (M)	Fracture Length (M)	Fracture Strike	Fracture Dip	Fracture Vector x coord	Fracture Vector y coord	Fracture Vector z coord	Weighting factor for fracture spacing		COS of angle between Scanline & Fracture Vector	Additional Notes
1	172	10.58	3.2258		260	70	-0.93	0.16	0.34	1.06		0.94	
		29.30	8.9306		254	90	-0.96	0.28	0.00	1.01		0.99	
2	342	14.55	4.4348		59	90	0.86	-0.52	0.00	1.03		0.97	
		30.33	9.2446		59	90	0.86	-0.52	0.00	1.03		0.97	
3	255	0.00	0		350	78	-0.17	-0.96	0.21	1.03		0.97	
		2.16	0.6596		350	72	-0.17	-0.94	0.31	1.06		0.95	
		4.42	1.346		359	79	-0.02	-0.98	0.19	1.05		0.95	
		7.41	2.26		342	87	-0.31	-0.95	0.05	1.00		1.00	
		13.50	4.1148		353	76	-0.12	-0.96	0.24	1.04		0.96	
		18.25	5.5626		348	90	-0.21	-0.98	0.00	1.00		1.00	
		25.67	7.8232		348	74	-0.20	-0.94	0.28	1.04		0.96	
		28.17	8.5852		355	83	-0.09	-0.99	0.12	1.02		0.98	
4	273	0.00	0		2	85	0.03	-1.00	0.09	1.00		1.00	
		3.83	1.1684		1	90	0.02	-1.00	0.00	1.00		1.00	
		6.67	2.032		348	82	-0.21	-0.97	0.14	1.05		0.96	
		11.00	3.3538		354	90	-0.10	-0.99	0.00	1.01		0.99	
5	265	2.00	0.6096		351	90	-0.16	-0.99	0.00	1.00		1.00	
										Total Fracture Density	0.511785758		

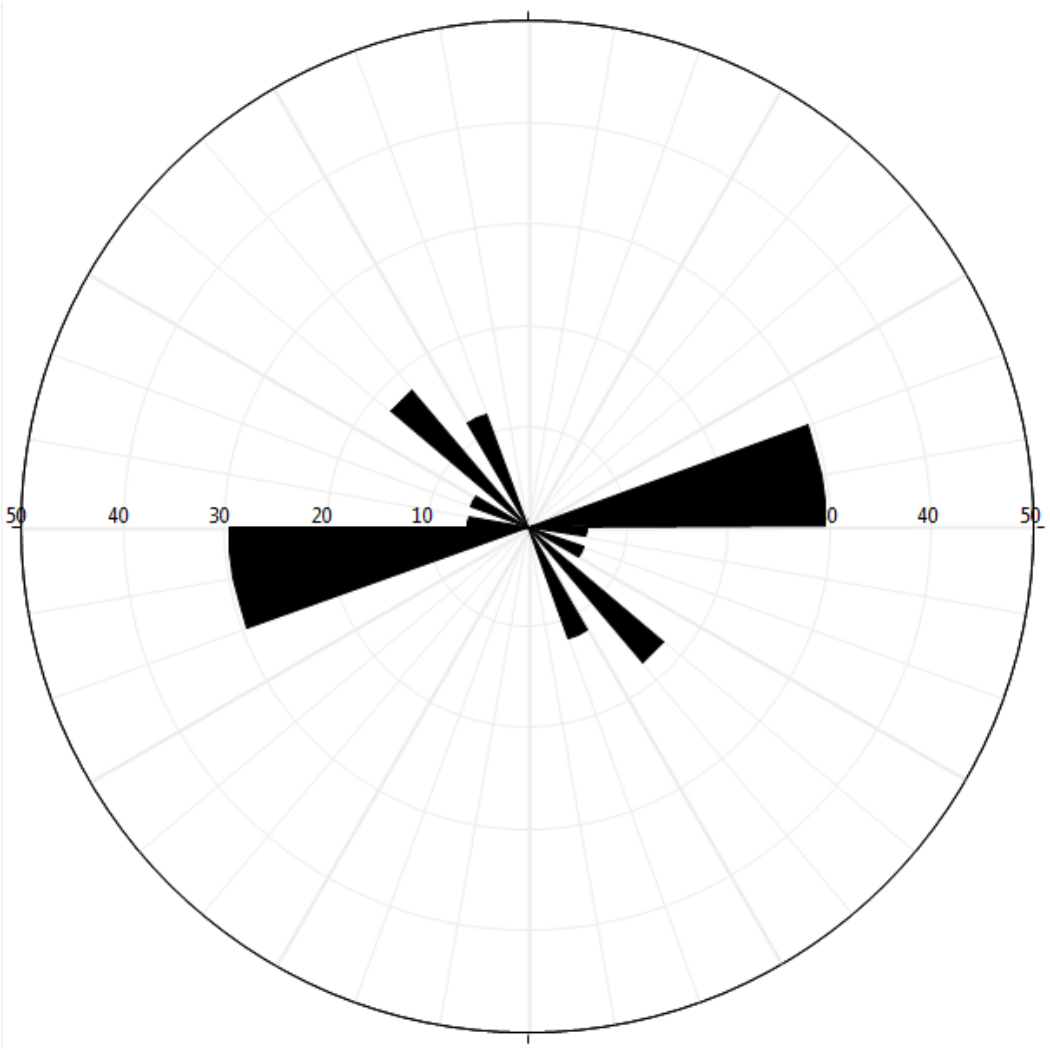

Figure 4-3. Rose Diagram of mode I fractures in the Quartermaster Formation within Palo Duro Canyon, TX

Table 4-2. Trujillo Formation Data – Station 2 - PD STA-2

Station	UTM Coordinates	Strike of Outcrop (Right Hand Rule)	Dip of Outcrop (Right Hand Rule)	Thickness of Bed (M)	Strike of Bed (Right Hand Rule)	Dip of Bed (Right Hand Rule)	Trend of Scanline	Plunge of scanline	Length of Scanline	Scanline Vector x = North	Scanline Vector y = East	Scanline Vector z = down	Sample #
Palo Duro 2	14R 254980 E 3873920 N +/- 6m	240	Horizontal	N/A	240	0	240	0	8.53	-0.50	-0.87	0.00	PD STA-2
						Scanline 1	240	0	8.53	-0.50	-0.87	0.00	
						Scanline 2	336	0	3.65	0.91	-0.41	0.00	

Scan Line #	Trend	Fracture Distance (ft)	Fracture Distance (M)	Fracture Length (M)	Fracture Strike	Fracture Dip	Fracture Vector x coord	Fracture Vector y coord	Fracture Vector z coord	Weighting factor for fracture spacing		COS of angle between Scanline & Fracture Vector	Additional Notes
1	240	1.25	0.381		340	90	-0.34	-0.94	0.00	1.02		0.98	
		6.08	1.8542		338	86	-0.37	-0.92	0.07	1.01		0.99	
		25.67	7.8232		341	90	-0.33	-0.95	0.00	1.02		0.98	
		36.08	10.9982		355	90	-0.09	-1.00	0.00	1.10		0.91	
		44.50	13.5636		347	90	-0.22	-0.97	0.00	1.05		0.96	
		47.75	14.5542		337	82	-0.39	-0.91	0.14	1.02		0.98	
		48.83	14.8844		322	84	-0.61	-0.78	0.10	1.02		0.98	
2	336	2.67	0.8128		63	78	0.87	-0.44	0.21	1.02		0.98	
		10.00	3.048		60	85	0.86	-0.50	0.09	1.01		0.99	
		36.33	11.0744		72	90	0.95	-0.31	0.00	1.01		0.99	
										Total Fracture Density	0.842931747		

Table 4-3. Trujillo Formation Data – Station 3 - PD STA-3

Station	UTM Coordinates	Strike of Outcrop (Right Hand Rule)	Dip of Outcrop (Right Hand Rule)	Thickness of Bed (M)	Strike of Bed (Right Hand Rule)	Dip of Bed (Right Hand Rule)	Trend of Scanline	Plunge of scanline	Length of Scanline (M)	Scanline Vector x = North	Scanline Vector y = East	Scanline Vector z = down	Sample #
PD STA-3	14S 256301 E 3870634 N +/- 4 meters	172	Horizontal	3.048	172	Horizontal	172	0	16.7	-0.99	0.14	0.00	PD STA-3

Scan Line #	Trend	Fracture Distance (ft)	Fracture Distance (M)	Fracture Length (M)	Fracture Strike	Fracture Dip	Fracture Vector x coord	Fracture Vector y coord	Fracture Vector z coord	Weighting factor for fracture spacing		COS of angle between Scanline & Fracture Vector	Additional Notes
1	172	0.00	0		150	90	0.50	0.87	0.00	2.67		-0.37	
		1.70	0.51816		150	90	0.50	0.87	0.00	2.67		-0.37	
		8.60	2.62128		89	76	0.97	-0.02	0.24	1.04		-0.96	
		9.25	2.8194		132	90	0.74	0.67	0.00	1.56		-0.64	
		12.80	3.90144		71	90	0.95	-0.33	0.00	1.02		-0.98	
		17.00	5.1816		75	90	0.97	-0.26	0.00	1.01		-0.99	
		24.60	7.49808		76	90	0.97	-0.24	0.00	1.01		-0.99	
		31.70	9.66216		80	81	0.97	-0.17	0.16	1.01		-0.99	
		33.25	10.1346		90	73	0.96	0.00	0.29	1.06		-0.95	
		33.00	10.0584		89	90	1.00	-0.02	0.00	1.01		-0.99	
		36.25	11.049		77	90	0.97	-0.22	0.00	1.00		-1.00	
		40.50	12.3444		80	90	0.98	-0.17	0.00	1.00		-1.00	
		42.09	12.829032		82	85	0.99	-0.14	0.09	1.00		-1.00	
		42.25	12.8778		110	90	0.94	0.34	0.00	1.13		-0.88	
		45.45	13.85316		135	90	0.71	0.71	0.00	1.66		-0.60	
		47.50	14.478		130	90	0.77	0.64	0.00	1.49		-0.67	
		51.09	15.572232		72	87	0.95	-0.31	0.05	1.02		-0.98	
										Total Fracture Density	1.338626519		

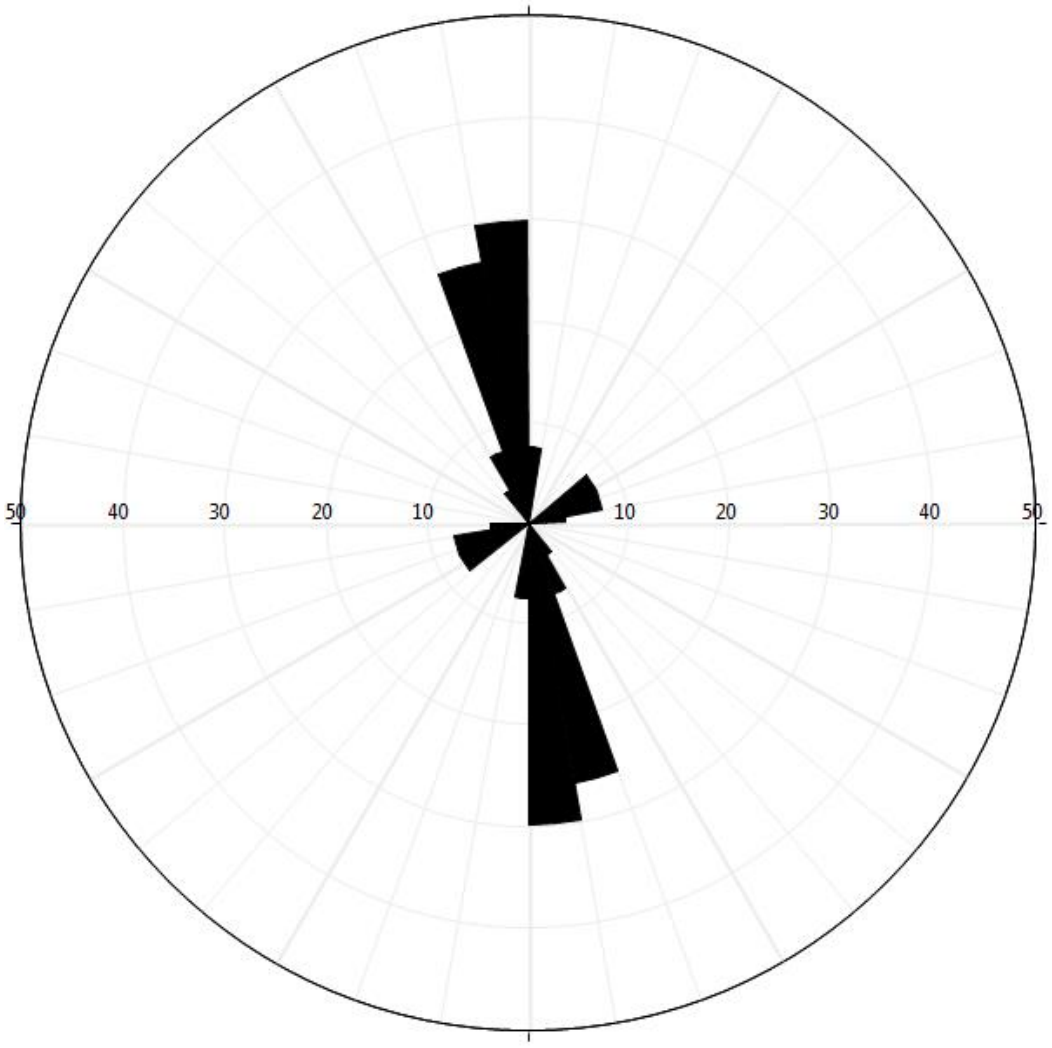

Figure 4-4. Rose Diagram of the Trujillo Formation within Palo Duro Canyon, TX

4.1.2 Bighorn Basin, WY

Only the Bighorn Dolomite (Figure 4-5) was measured around Sheep Mountain Anticline due to the limited exposures of mode I jointing. Two stations, BH STA 1 and BH STA 2, were taken from one outcrop but different beds of the formation. All of the fracture density data can be viewed in Table 5 (BH STA-1) and Table 6 (BH STA-2).

Using one scanline of 75 feet and trending at 81° NE, the fracture density for BH STA-1 measured 1.196 m^{-1}. Only one scanline was used for BH STA-2 as well, trending 105° NE with an overall length of 50 feet. The measured fracture density for BH STA-2 was 1.464 m^{-1}. The primary joint orientations for both stations were approximately NW and SW (Figure 4-6).

Figure 4-5. Bighorn Dolomite – Station BH STA-1

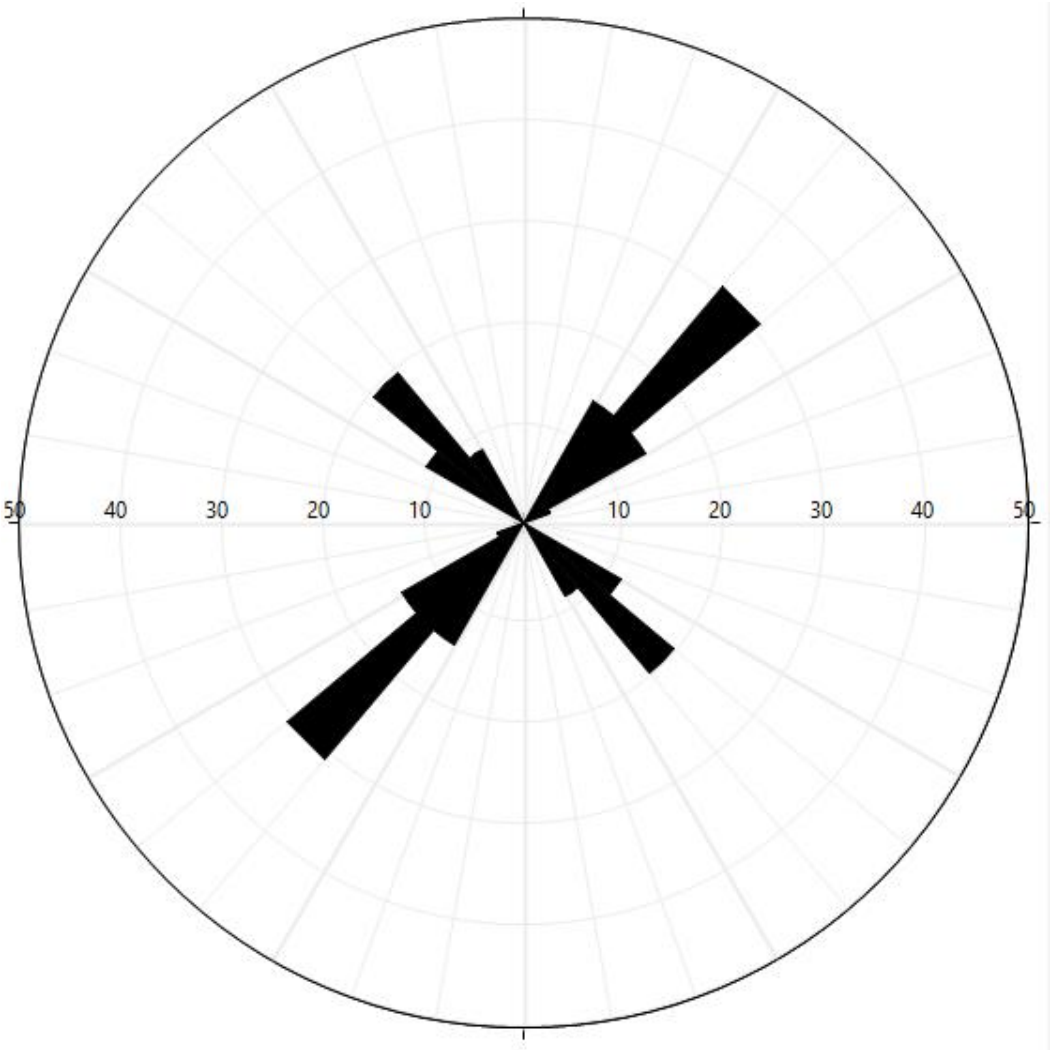

Figure 4-6. Rose Diagram of stations BH STA-1 and BH STA-2, Bighorn Dolomite

Table 4-4. Bighorn Dolomite Data – Station 1 – BH STA-1

Station	UTM Coordinates	Strike of Outcrop (Right Hand Rule)	Dip of Outcrop (Right Hand Rule)	Thickness of Bed (M)	Strike of Bed (Right Hand Rule)	Dip of Bed (Right Hand Rule)	Trend of Scanline	Plunge of scanline	Length of Scanline (M)	Scanline Vector x = North	Scanline Vector y = East	Scanline Vector z = down	Sample #
BH STA-1	12S 723129 N 4950372 N +/- 4 meters		Horizontal	1.64 to 3.28	133	Horizontal	81	0	24.6	0.16	0.99	0.00	BH STA-1
						Scanline 1	81	0	24.6	0.16	0.99	0.00	

Scan Line #	Trend	Fracture Distance (ft)	Fracture Distance (M)	Fracture Length (M)	Fracture Strike	Fracture Dip	Fracture Vector x coord	Fracture Vector y coord	Fracture Vector z coord	Weighting factor for fracture spacing		COS of angle between Scanline & Fracture Vector	Additional Notes
1	81	0.00	0		231	90	-0.78	0.63	0.00	2.00		0.50	
		6.20	2.0336		310	90	-0.77	-0.64	0.00	1.33		-0.75	
		6.70	2.1976		219	89	-0.63	0.78	0.02	1.49		0.67	
		13.50	4.428		327	89	-0.54	-0.84	0.02	1.09		-0.91	
		14.20	4.6576		307	90	-0.80	-0.60	0.00	1.39		-0.72	
		15.80	5.1824		224	87	-0.69	0.72	0.05	1.66		0.60	
		17.70	5.8056		324	82	-0.58	-0.80	0.14	1.13		-0.88	
		19.00	6.232		229	85	-0.75	0.65	0.09	1.89		0.53	
		25.70	8.4296		307	88	-0.80	-0.60	0.03	1.39		-0.72	
		19.30	6.3304		228	90	-0.74	0.67	0.00	1.84		0.54	
		23.70	7.7736		233	81	-0.79	0.59	0.16	2.16		0.46	
		34.40	11.2832		310	90	-0.77	-0.64	0.00	1.33		-0.75	
		34.70	11.3816		317	87	-0.68	-0.73	0.05	1.21		-0.83	
		36.90	12.1032		229	88	-0.75	0.66	0.03	1.89		0.53	
		43.30	14.2024		317	85	-0.68	-0.73	0.09	1.21		-0.83	
		45.00	14.76		320	90	-0.64	-0.77	0.00	1.17		-0.86	
		59.10	19.3848		233	90	-0.80	0.60	0.00	2.13		0.47	
		67.95	22.2876		245	90	-0.906307787	0.422618262	0	3.63		0.28	
		71.50	23.452		224	90	-0.69	0.72	0.00	1.66		0.60	
		72.90	23.9112		316	90	-0.69	-0.72	0.00	1.22		-0.82	
										Total Fracture Density	1.3341034		

Table 4-5. . Bighorn Dolomite Data – Station 2 – BH STA-2

Station	UTM Coordinates	Strike of Outcrop (Right Hand Rule)	Dip of Outcrop (Right Hand Rule)	Thickness of Bed (M)	Strike of Bed (Right Hand Rule)	Dip of Bed (Right Hand Rule)	Trend of Scanline	Plunge of scanline	Length of Scanline	Scanline Vector x = North	Scanline Vector y = East	Scanline Vector z = down	Sample #
BH STA-2	12 S 723144 N 4950382 N +/- 5m		Horizontal	2.5	94	10	105	0	16.4	-0.26	0.97	0.00	BH STA-2
						Scanline 1	240	0	16.4	-0.26	0.97	0.00	

Scan Line #	Trend	Fracture Distance (ft)	Fracture Distance (M)	Fracture Length (M)	Fracture Strike	Fracture Dip	Fracture Vector x coord	Fracture Vector y coord	Fracture Vector z coord	Weighting factor for fracture spacing		COS of angle between Scanline & Fracture Vector	Additional Notes
1	105	0.00	0		214	90	-0.56	0.83	0.00	1.06		0.95	
		1.60	0.5248		316	88	-0.69	-0.72	0.03	1.94		-0.51	
		4.00	1.312		304	87	-0.83	-0.56	0.05	3.08		-0.33	
		4.20	1.3776		219	90	-0.63	0.78	0.00	1.09		0.91	
		5.90	1.9352		309	85	-0.77	-0.63	0.09	2.47		-0.41	
		9.90	3.2472		311	83	-0.75	-0.65	0.12	2.30		-0.44	
		13.10	4.2968		223	90	-0.68	0.73	0.00	1.13		0.88	
		15.50	5.084		218	84	-0.61	0.78	0.10	1.09		0.92	
		19.00	6.232		229	90	-0.75	0.66	0.00	1.21		0.83	
		30.40	9.9712		229	85	-0.75	0.65	0.09	1.21		0.83	
		32.90	10.7912		230	90	-0.77	0.64	0.00	1.22		0.82	
		38.10	12.4968		236	88	-0.83	0.56	0.03	1.33		0.75	
		41.60	13.6448		226	90	-0.72	0.69	0.00	1.17		0.86	
		43.90	14.3992		222	89	-0.67	0.74	0.02	1.12		0.89	
		44.90	14.7272		226	90	-0.72	0.69	0.00	1.17		0.86	
		46.70	15.3176		218	88	-0.62	0.79	0.03	1.09		0.92	
										Total Fracture Density	1.376915749		

4.1.3 Highway 90 Road Cuts, Val Verde County, TX

Data was gathered from five formations along Highway 90: Lower Austin (Atco) Chalk, Boquillas Shale, Buda Limestone, Del Rio Clay, and Salmon Peak Limestone. Out of these five formations, twelve stations were measured for fracture density and 15 rock samples were taken for further lab analysis. Tables 7 through 19 display the field measurements for each locale. With the exception of station 13-12-14-1, only one scanline was used per station.

The first station, 13-12-14-1, was measured on the Salmon Peak Limestone (Table 4-6). 13-12-14-1 had a fracture density of 1.195 M^{-1} with a strike orientation of NW-SW (Figure 4-7). The next station, 13-12-14-2, was measured on the Buda Limestone where measurements produced a fracture density of 1.464 M^{-1} (Table 4-7). Strike orientations of the Buda Limestone were in the NE-NW directions (Figure 4-10). Station 13-12-14-3 was measured from a rather large roadcut exposing the Boquillas Shale. Measurements indicated a fracture density of 1.633 M^{-1} (Table 4-8) with joint orientations primarily in the NE-SW directions (Figure 4-17). Further on was the Atco Chalk, where Stations 13-12-14-4 through 13-12-14-7 had the following fracture densities: 13-12-14-4 had a fracture density of 0.591 M^{-1}; 13-12-14-5 had a fracture density of 0.757 M^{-1}; 13-12-14-6 had a fracture density of 1.556 M^{-1}; 13-12-14-7 had a fracture density of 1.352 M^{-1} (Tables 4-9 through 4-12). The overall strike orientation of the Atco Chalk was NE-SW (Figure 4-15).

Three more stations (14-12-14-1, 14-12-14-2, and 14-12-14-3) were generated at the exposed Boquillas Shale roadcut mentioned above. 14-12-14-1 had a fracture density of 1.615 M^{-1} (Table 4-13). 14-12-14-2 had a fracture density of 1.775 M^{-1} (Table 4-14). Finally, 14-12-14-3 had a fracture density of 2.202 M^{-1} (Table 4-15). Stations 14-12-14-1 through 14-12-14-3 had a strike orientation of NW-SW (Figure 4-17).

Station 14-12-14-4 was measured on the Del Rio formation, with a fracture density of 1.745 M^{-1} (Table 4-16). Fractures were striking primarily SE (Figure 4-18). The final station, 14-12-14-5, was measured on the Salmon Peak Limestone with a fracture density of 1.506 M^{-1} (Table 4-17). Its primary strike orientation is shown in Figure 4-15.

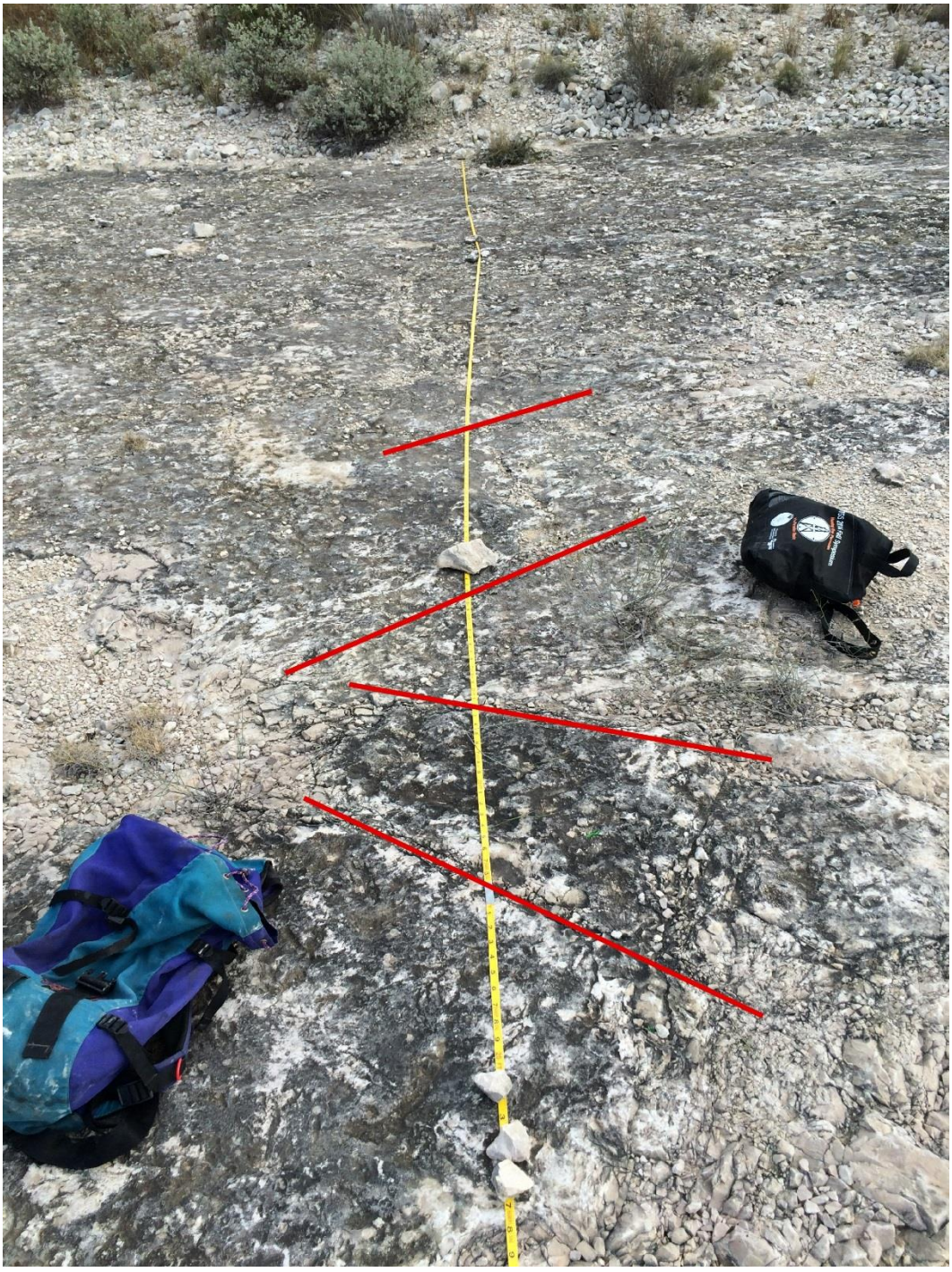

Figure 4-7. Salmon Peak Limestone – Station 13-12-14-1; Red lines designate fractures crossing the scanline

Table 4-6. Salmon Peak Limestone Data – 13-12-14-1 – Station 1

Station	UTM Coordinates	Strike of Outcrop (Right Hand Rule)	Dip of Outcrop (Right Hand Rule)	Thickness of Bed (M)	Strike of Bed (Right Hand Rule)	Dip of Bed (Right Hand Rule)	Trend of Scanline	Plunge of scanline	Length of Scanline	Scanline Vector x = North	Scanline Vector y = East	Scanline Vector z = down	Sample #	Sample strike (right hand rule)
13-12-14-1	14R 302535 E 3264220 N +/- 3m	306	7	N/A	306	0	306	7	28.04	0.58	-0.80	0.12	13-12-14-1	N/A
						Scanline 1	306	7	28.0416	0.58	-0.80	0.12		
						Scanline 2	224	3	7.9248	-0.72	-0.69	0.05		
						Scanline 3	224	3	8.2296	-0.72	-0.69	0.05		
						Scanline 4	224	3	6.4008	-0.72	-0.69	0.05		

Scan Line #	Trend	Fracture Distance (ft)	Fracture Distance (M)	Fracture Length (M)	Fracture Strike	Fracture Dip	Fracture Vector x coord	Fracture Vector y coord	Fracture Vector z coord	Weighting factor for fracture spacing		COS of angle between Scanline & Fracture Vector	Fracture Length (ft)	Additional Notes
1	306	0.5	0.1524	3.6576	205	52.00	-0.33	0.71	0.62	1.44		-0.69	12	
		23.1	7.04088	0.6096	28	39	0.30	-0.56	0.78	1.40		0.71	2	
		23.6	7.19328	0.6096	208	20	-0.16	0.30	0.94	4.51		-0.22	2	
		30.95	9.43356	5.4864	207	76	-0.44	0.86	0.24	1.08		-0.92	18	
		69.15	21.07692	1.3716	219	90	-0.63	0.78	0.00	1.01		-0.99	4.5	
		77.4	23.59152	0.4572	275	90	-1.00	-0.09	0.00	1.96		-0.51	1.5	
		79.05	24.09444	1.2192	264	90	-0.99	0.10	0.00	1.51		-0.66	4	
		84.8	25.84704	0.6096	239	90	-0.86	0.52	0.00	1.09		-0.91	2	
		87.8	26.76144	0.762	326	90	-0.56	-0.83	0.00	2.95		0.34	2.5	
		89.5	27.2796	0.3048	216	90	-0.59	0.81	0.00	1.01		-0.99	1	
		91.5	27.8892	0.9144	186	90	-0.10	0.99	0.00	1.16		-0.86	3	
		92	28.0416	0.3048	194	90	-0.24	0.97	0.00	1.09		-0.92	1	
2	224	0.7	0.21336	4.2672	294	90	-0.91	-0.41	0.00	1.07		0.94	14	
		7.05	2.14884	1.524	280	90	-0.98	-0.17	0.00	1.21		0.83	5	
		8.1	2.46888	0.4572	273	90	-1.00	-0.05	0.00	1.33		0.75	1.5	
		9.6	2.92608	6.7056	294	90	-0.91	-0.41	0.00	1.07		0.94	22	
		15.3	4.66344	2.5908	294	90	-0.91	-0.41	0.00	1.07		0.94	8.5	
		17.2	5.24256	15.8496	299	90	-0.87	-0.48	0.00	1.04		0.96	52	
		20.7	6.30936	3.3528	280	90	-0.98	-0.17	0.00	1.21		0.83	11	
		21.7	6.61416	2.7432	304	90	-0.83	-0.56	0.00	1.02		0.98	9	
		21.9	6.67512	0.9144	306	90	-0.81	-0.59	0.00	1.01		0.99	3	
		22.1	6.73608	0.9144	308	90	-0.79	-0.62	0.00	1.01		0.99	3	
		23.8	7.25424	1.3716	353	90	-0.12	-0.99	0.00	1.29		0.78	4.5	
		26	7.9248	1.524	306	90	-0.81	-0.59	0.00	1.01		0.99	5	
3	224	4.9	1.49352	3.6576	314	90	-0.72	-0.69	0.00	1.00		1.00	12	
		20.6	6.27888	1.524	310	90	-0.77	-0.64	0.00	1.00		1.00	5	
		21.75	6.6294	1.7526	307	90	-0.80	-0.60	0.00	1.01		0.99	5.75	
		22.2	6.76656	0.9144	312	90	-0.74	-0.67	0.00	1.00		1.00	3	
		23.45	7.14756	1.9812	342	90	-0.31	-0.95	0.00	1.13		0.88	6.5	
4	224	16.4	4.99872	0.9144	329	90	-0.52	-0.86	0.00	1.04		0.96	3	
		17.4	5.30352	1.2192	322	90	-0.62	-0.79	0.00	1.01		0.99	4	
		18.8	5.73024	0.762	324	90	-0.59	-0.81	0.00	1.02		0.98	2.5	
		18.9	5.76072	1.8288	317	90	-0.68	-0.73	0.00	1.00		1.00	6	
		19.25	5.8674	0.4572	317	90	-0.68	-0.73	0.00	1.00		1.00	1.5	
		20.2	6.15696	0.4572	293	90	-0.92	-0.39	0.00	1.07		0.93	1.5	
		20.45	6.23316	0.3048	296	90	-0.90	-0.44	0.00	1.05		0.95	1	
										Total Fracture Density	1.195491474			

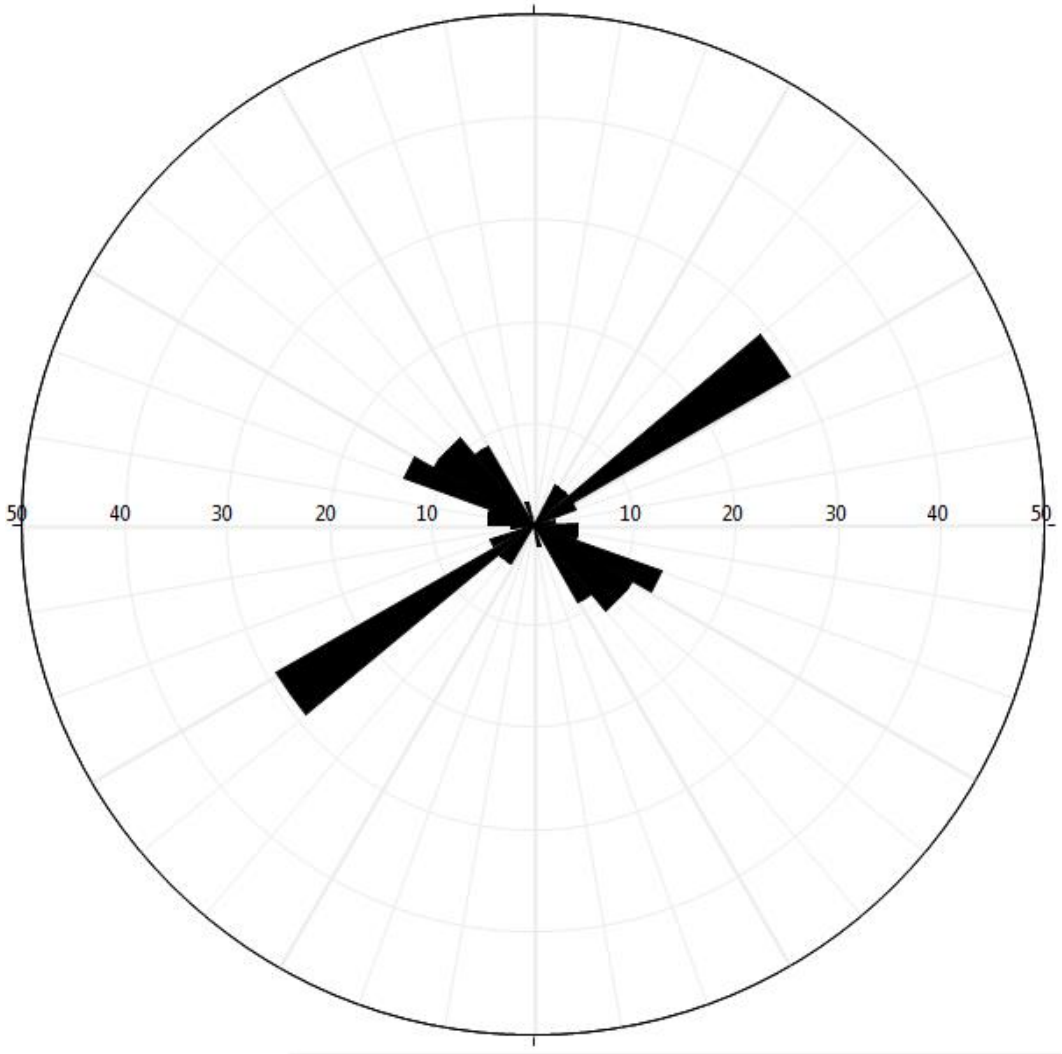

Figure 4-8. Rose Diagram of station 13-12-14-1 and 14-12-14-5, Salmon Peak Limestone

Figure 4-9. Buda Limestone – Station 13-12-14-2

Table 4-7. Buda Formation Data – 13-12-14-2 – Station 2

Station	UTM Coordinates	Strike of Outcrop (Right Hand Rule)	Dip of Outcrop (Right Hand Rule)	Thickness of Bed (M)	Strike of Bed (Right Hand Rule)	Dip of Bed (Right Hand Rule)	Trend of Scanline	Plunge of scanline	Length of Scanline	Scanline Vector x = North	Scanline Vector y = East	Scanline Vector z = down	Sample #	Sample strike (right hand rule)
13-12-14-2	14R 291958 E 3283132 N +/- 4m	345	90	N/A	345	0	345	0	22.86	0.97	-0.26	0.00	13-12-14-2	N/A

Scan Line #	Trend	Fracture Distance (ft)	Fracture Distance (M)	Fracture Length (M)	Fracture Strike	Fracture Dip	Fracture Vector x coord	Fracture Vector y coord	Fracture Vector z coord	Weighting factor for fracture spacing		COS of angle between Scanline & Fracture Vector	Fracture Length (ft)	Additional Notes
1	345	1.5	0.4572	1.524	20	87.00	0.34	-0.94	0.05	1.75		0.57	5	
		3.2	0.97536	1.2192	42	87	0.67	-0.74	0.05	1.19		0.84	4	
		6.7	2.04216	2.7432	209	85	-0.48	0.87	0.09	1.45		-0.69	9	
		8.6	2.62128	1.524	175	90	0.09	1.00	0.00	5.76		-0.17	5	
		23.9	7.28472	0.9144	182	90	-0.03	1.00	0.00	3.42		-0.29	3	
		25.9	7.89432	2.4384	180	89	0.00	1.00	0.02	3.86		-0.26	8	
		33.8	10.30224	2.7432	292	90	-0.93	-0.37	0.00	1.25		-0.80	9	
		40.6	12.37488	2.7432	43	79	0.67	-0.72	0.19	1.20		0.83	9	
		45.4	13.83792	2.7432	58	77	0.83	-0.52	0.22	1.07		0.93	9	
		49.7	15.14856	0.3048	325	90	-0.57	-0.82	0.00	2.92		-0.34	1	
		54.9	16.73352	1.8288	255	90	-0.97	0.26	0.00	1.00		-1.00	6	
		58.2	17.73936	0.6096	40	90	0.64	-0.77	0.00	1.22		0.82	2	
		61.3	18.68424	1.524	297	90	-0.89	-0.45	0.00	1.35		-0.74	5	
		64.9	19.78152	1.2192	62	90	0.88	-0.47	0.00	1.03		0.97	4	
		66.9	20.39112	0.1524	60	90	0.87	-0.50	0.00	1.04		0.97	0.5	
		69.9	21.30552	0.9144	242	84	-0.88	0.47	0.10	1.03		-0.97	3	
		70.4	21.45792	1.8288	5	87	0.09	-0.99	0.05	2.93		0.34	6	
										Total Fracture Density	1.463972384			

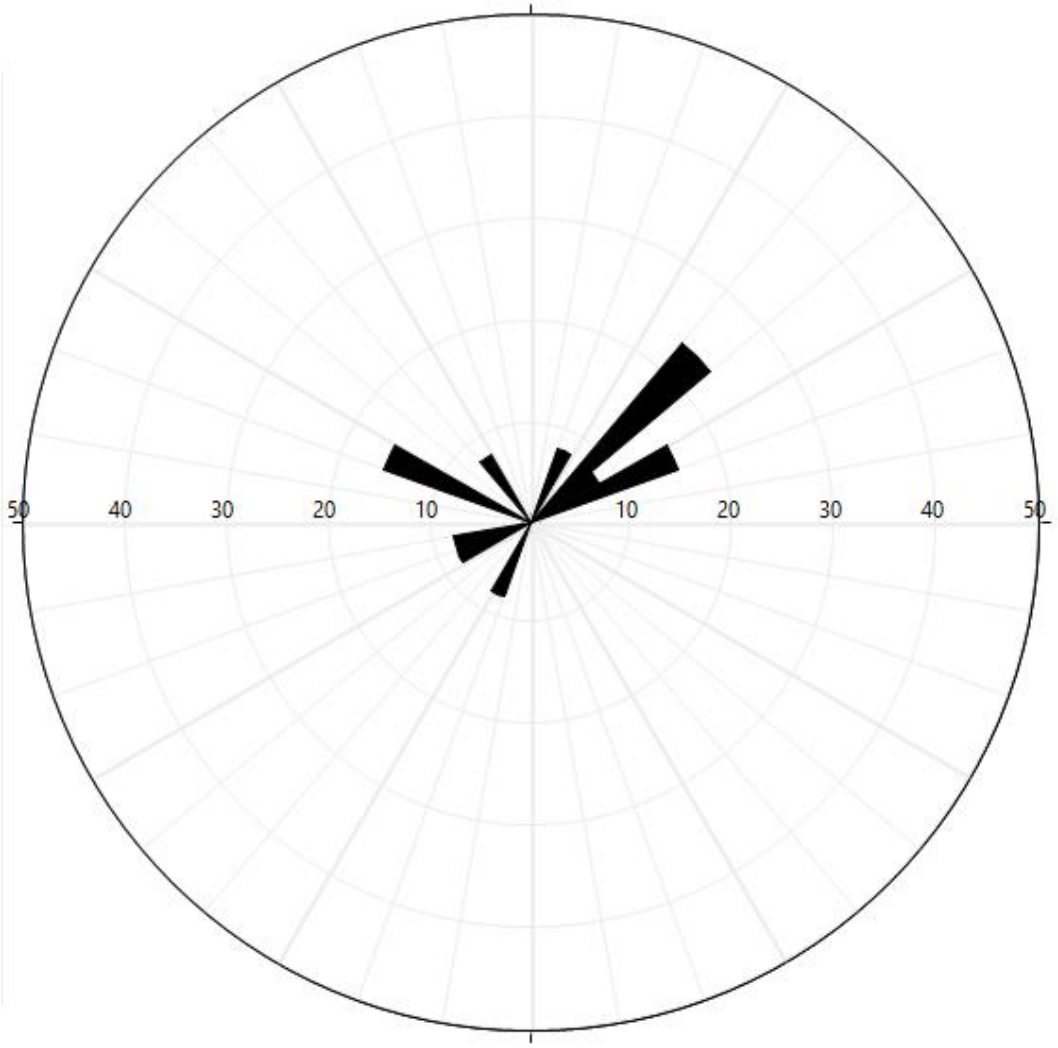

Figure 4-10. Rose Diagram of station 13-12-14-2, Buda Limestone

Figure 4-11. Boquillas Shale – Station 13-12-14-3; Gray areas indicate high organic content

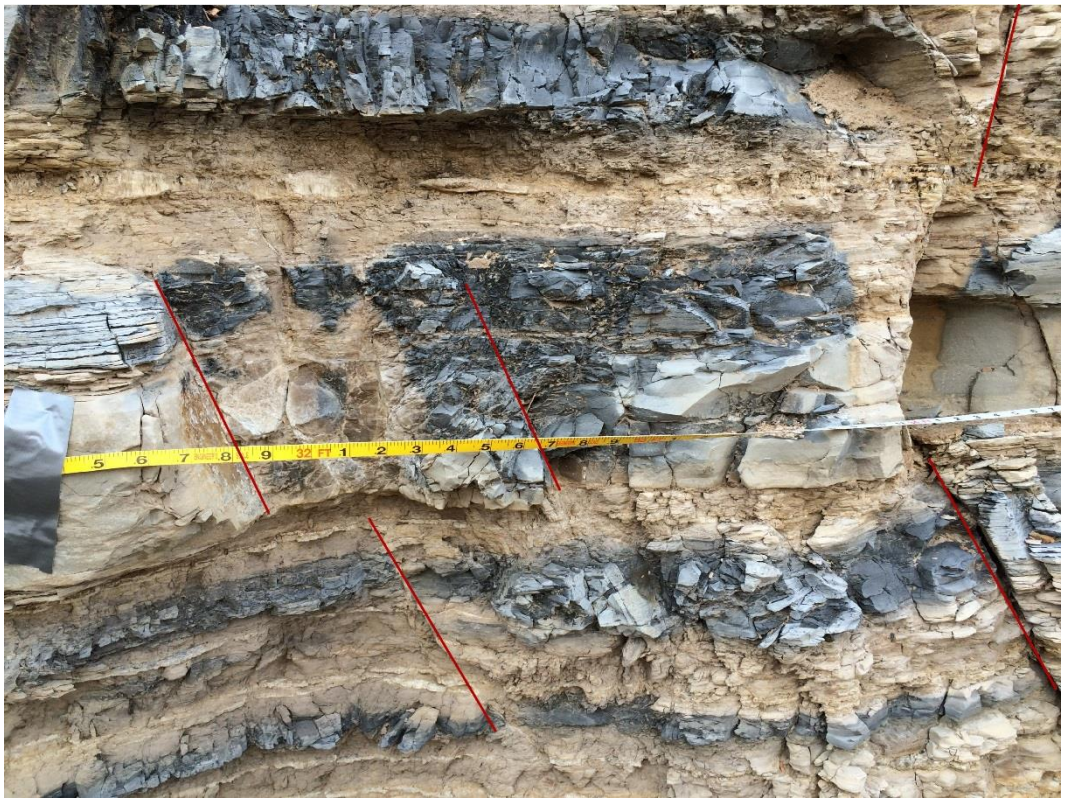

Figure 4-12. Boquillas Shale – Station 13-12-14-3; Red lines indicate fractures

Table 4-8. Boquillas Shale Data – 13-12-14-3 – Station 3

Station	UTM Coordinates	Strike of Outcrop (Right Hand Rule)	Dip of Outcrop (Right Hand Rule)	Thickness of Bed (M)	Strike of Bed (Right Hand Rule)	Dip of Bed (Right Hand Rule)	Trend of Scanline	Plunge of scanline	Length of Scanline	Scanline Vector x = North	Scanline Vector y = East	Scanline Vector z = down	Sample #	Sample strike (right hand rule)
13-12-14-3	14R 291958 E 3283132 N +/- 4m	283	8	1.524	283	0	283	0	15.24	0.22	-0.97	0.00	13-12-14-3	N/A

Scan Line #	Trend	Fracture Distance (ft)	Fracture Distance (M)	Fracture Length (M)	Fracture Strike	Fracture Dip	Fracture Vector x coord	Fracture Vector y coord	Fracture Vector z coord	Weighting factor for fracture spacing		COS of angle between Scanline & Fracture Vector	Fracture Length (ft)	Additional Notes
1	238	6.4	1.95072	1.524	297	81	-0.88	-0.45	0.16	4.19		0.24	5	
		8.6	2.62128	0.6096	197	90	-0.29	0.96	0.00	1.00		-1.00	2	
		8.9	2.71272	1.2192	64	82	0.89	-0.43	0.14	1.60		0.62	4	
		10.7	3.26136	0.6096	221	86	-0.65	0.75	0.07	1.14		-0.88	2	
		13.3	4.05384	0.9144	216	90	-0.59	0.81	0.00	1.09		-0.92	3	
		16.95	5.16636	1.524	240	90	-0.87	0.50	0.00	1.47		-0.68	5	
		23	7.0104	0.3048	220	90	-0.64	0.77	0.00	1.12		-0.89	1	
		28.3	8.62584	1.524	312	81	-0.73	-0.66	0.16	2.09		0.48	5	
		28.7	8.74776	0.9144	226	84	-0.72	0.69	0.10	1.20		-0.83	3	
		30.7	9.35736	1.524	150	88	0.50	0.87	0.03	1.37		-0.73	5	
		36	10.9728	1.524	135	62	0.62	0.62	0.47	2.14		-0.47	5	
		32.8	9.99744	1.524	230	88	-0.77	0.64	0.03	1.25		-0.80	5	
		43	13.1064	1.524	120	85	0.86	0.50	0.09	3.43		-0.29	5	
		45.3	13.80744	0.3048	145	56	0.48	0.68	0.56	1.80		-0.55	1	
										Total Fracture Density	1.632816084			

Figure 4-13. Atco Chalk – Stations 4 through 7

Figure 4-14. Atco Chalk – Stations 13-12-14-4 through 13-12-14-7; Close-up reveals calcite filling in open fractures

Table 4-9. Atco Chalk Data – 13-12-14-4 – Station 4

Station	UTM Coordinates	Strike of Outcrop (Right Hand Rule)	Dip of Outcrop (Right Hand Rule)	Thickness of Bed (M)	Strike of Bed (Right Hand Rule)	Dip of Bed (Right Hand Rule)	Trend of Scanline	Plunge of scanline	Length of Scanline	Scanline Vector x = North	Scanline Vector y = East	Scanline Vector z = down	Sample #	Sample strike (right hand rule)
13-12-14-4	14R 246149 E 3302898 N +/- 4m	114	74	1.524	114	0	114	0	18.288	-0.41	0.91	0.00	13-12-14-4	N/A

Scan Line #	Trend	Fracture Distance (ft)	Fracture Distance (M)	Fracture Length (M)	Fracture Strike	Fracture Dip	Fracture Vector x coord	Fracture Vector y coord	Fracture Vector z coord	Weighting factor for fracture spacing		COS of angle between Scanline & Fracture Vector	Fracture Length (ft)	Additional Notes
1	114	0.3	0.09144	1.524	34	90	0.56	-0.83	0.00	1.02		-0.98	5	
		4.2	1.28016	0.9144	48	90	0.74	-0.67	0.00	1.09		-0.91	3	
		4.6	1.40208	1.524	35	90	0.57	-0.82	0.00	1.02		-0.98	5	
		6.3	1.92024	0.9144	39	90	0.63	-0.78	0.00	1.04		-0.97	3	
		15.9	4.84632	1.524	32	90	0.53	-0.85	0.00	1.01		-0.99	5	
		20.5	6.2484	1.524	47	90	0.73	-0.68	0.00	1.09		-0.92	5	
		24.75	7.5438	1.524	50	90	0.77	-0.64	0.00	1.11		-0.90	5	
		30.95	9.43356	1.524	51	90	0.78	-0.63	0.00	1.12		-0.89	5	
		53	16.1544	0.9144	56	90	0.83	-0.56	0.00	1.18		-0.85	3	
		53.15	16.20012	1.524	52	90	0.79	-0.62	0.00	1.13		-0.88	5	
										Total Fracture Density	0.59092959			

Table 4-10. Atco Chalk Data – 13-12-14-5 – Station 5

Station	UTM Coordinates	Strike of Outcrop (Right Hand Rule)	Dip of Outcrop (Right Hand Rule)	Thickness of Bed (M)	Strike of Bed (Right Hand Rule)	Dip of Bed (Right Hand Rule)	Trend of Scanline	Plunge of scanline	Length of Scanline	Scanline Vector x = North	Scanline Vector y = East	Scanline Vector z = down	Sample #	Sample strike (right hand rule)
13-12-14-5	14R 246083 E 3302938 N +/- 4m	109	64	0.9144	109	0	109	0	16.1544	-0.33	0.95	0.00	13-12-14-4	N/A

Scan Line #	Trend	Fracture Distance (ft)	Fracture Distance (M)	Fracture Length (M)	Fracture Strike	Fracture Dip	Fracture Vector x coord	Fracture Vector y coord	Fracture Vector z coord	Weighting factor for fracture spacing		COS of angle between Scanline & Fracture Vector	Fracture Length (ft)	Additional Comments
1	109	5.1	1.55448	0.9144	336	90	-0.41	-0.91	0.00	1.37		-0.73	3	
		15	4.572	0.9144	30	90	0.50	-0.87	0.00	1.02		-0.98	3	
		26.4	8.04672	0.9144	49	90	0.75	-0.66	0.00	1.15		-0.87	3	
		26.55	8.09244	0.3048	51	90	0.78	-0.63	0.00	1.18		-0.85	1	
		34.9	10.63752	0.9144	16	90	0.28	-0.96	0.00	1.00		-1.00	3	
		41.1	12.52728	0.9144	37	90	0.60	-0.80	0.00	1.05		-0.95	3	
		41	12.4968	0.9144	36	90	0.59	-0.81	0.00	1.05		-0.96	3	
		41.4	12.61872	0.9144	35	90	0.57	-0.82	0.00	1.04		-0.96	3	
		45.2	13.77696	0.9144	44	90	0.69	-0.72	0.00	1.10		-0.91	3	
		47.5	14.478	0.9144	47	90	0.73	-0.68	0.00	1.13		-0.88	3	
		50.6	15.42288	0.9144	47	90	0.73	-0.68	0.00	1.13		-0.88	3	
										Total Fracture Density	0.756900094			

Table 4-11. Atco Chalk Data – 13-12-14-6 – Station 6

Station	UTM Coordinates	Strike of Outcrop (Right Hand Rule)	Dip of Outcrop (Right Hand Rule)	Thickness of Bed (M)	Strike of Bed (Right Hand Rule)	Dip of Bed (Right Hand Rule)	Trend of Scanline	Plunge of scanline	Length of Scanline	Scanline Vector x = North	Scanline Vector y = East	Scanline Vector z = down	Sample #
13-12-14-6	14R 245950 E 3302989 N +/- 2m	105	65	0.9144	105	0	105	0	15.24	-0.26	0.97	0.00	13-12-14-6

Scan Line #	Trend	Fracture Distance (ft)	Fracture Distance (M)	Fracture Length (M)	Fracture Strike	Fracture Dip	Fracture Vector x coord	Fracture Vector y coord	Fracture Vector z coord	Weighting factor for fracture spacing		COS of angle between Scanline & Fracture Vector	Fracture Length (ft)
1	105	0.75	0.2286	0.9144	24	64	0.37	-0.82	0.44	1.13		-0.89	3
		0.8	0.24384	0.9144	24	59	0.35	-0.78	0.52	1.18		-0.85	3
		3.8	1.15824	0.9144	11	90	0.19	-0.98	0.00	1.00		-1.00	3
		4.8	1.46304	0.9144	14	90	0.24	-0.97	0.00	1.00		-1.00	3
		8.45	2.57556	0.9144	165	73	0.25	0.92	0.29	1.21		0.83	3
		9.75	2.9718	0.6096	11	90	0.19	-0.98	0.00	1.00		-1.00	2
		15.3	4.66344	0.9144	11	90	0.19	-0.98	0.00	1.00		-1.00	3
		16.8	5.12064	0.6096	17	90	0.29	-0.96	0.00	1.00		-1.00	2
		17.4	5.30352	0.9144	210	70	-0.47	0.81	0.34	1.10		0.91	3
		19.2	5.85216	0.6096	30	68	0.46	-0.80	0.37	1.12		-0.90	2
		22.55	6.87324	0.3048	20	90	0.34	-0.94	0.00	1.00		-1.00	1
		23	7.0104	0.9144	200	66	-0.31	0.86	0.41	1.10		0.91	3
		29.2	8.90016	0.9144	22	90	0.37	-0.93	0.00	1.01		-0.99	3
		30.1	9.17448	0.9144	23	90	0.39	-0.92	0.00	1.01		-0.99	3
		30.8	9.38784	0.9144	20	90	0.34	-0.94	0.00	1.00		-1.00	3
		33.8	10.30224	0.9144	25	90	0.42	-0.91	0.00	1.02		-0.98	3
		39.4	12.00912	0.9144	70	90	0.94	-0.34	0.00	1.74		-0.57	3
		40.25	12.2682	0.9144	0.00	74.00	0.00	-0.96	0.28	1.08		-0.93	3
		43.1	13.13688	0.9144	11.00	90.00	0.19	-0.98	0.00	1.00		-1.00	3
		43.8	13.35024	0.9144	21.00	90.00	0.36	-0.93	0.00	1.01		-0.99	3
		46.85	14.27988	0.3048	19.00	90.00	0.33	-0.95	0.00	1.00		-1.00	1
		49	14.9352	0.9144	18.00	90.00	0.31	-0.95	0.00	1.00		-1.00	3
										Total Fracture Density	1.55596612		

Table 4-12. Atco Chalk Data – 13-12-14-7 – Station 7

Station	UTM Coordinates	Strike of Outcrop (Right Hand Rule)	Dip of Outcrop (Right Hand Rule)	Thickness of Bed (M)	Strike of Bed (Right Hand Rule)	Dip of Bed (Right Hand Rule)	Trend of Scanline	Plunge of scanline	Length of Scanline	Scanline Vector x = North	Scanline Vector y = East	Scanline Vector z = down	Sample #	Sample strike (right hand rule)
13-12-14-7	14R 245789 E 3303012 N +/- 3m	273	72	0.6096	273	0	273	0	13.716	0.05	-1.00	0.00	13-12-14-7	N/A

Scan Line #	Trend	Fracture Distance (ft)	Fracture Distance (M)	Fracture Length (M)	Fracture Strike	Fracture Dip	Fracture Vector x coord	Fracture Vector y coord	Fracture Vector z coord	Weighting factor for fracture spacing		COS of angle between Scanline & Fracture Vector	Fracture Length (ft)	Additional Notes
1	273	0.8	0.24384	0.6096	212	90	-0.53	0.85	0.00	1.14		-0.87	2	
		5.2	1.58496	0.6096	210	90	-0.50	0.87	0.00	1.12		-0.89	2	
		6	1.8288	0.6096	240	90	-0.87	0.50	0.00	1.84		-0.54	2	
		9.4	2.86512	0.6096	215	86	-0.57	0.82	0.07	1.18		-0.85	2	
		10.4	3.16992	0.3048	217	78	-0.59	0.78	0.21	1.23		-0.81	1	
		15.2	4.63296	0.6096	206	90	-0.44	0.90	0.00	1.09		-0.92	2	
		16	4.8768	0.6096	207	90	-0.45	0.89	0.00	1.09		-0.91	2	
		20.5	6.2484	0.6096	209	90	-0.48	0.87	0.00	1.11		-0.90	2	
		22.15	6.75132	0.6096	198	90	-0.31	0.95	0.00	1.04		-0.97	2	
		26.2	7.98576	0.6096	220	90	-0.64	0.77	0.00	1.25		-0.80	2	
		30.2	9.20496	0.6096	202	90	-0.37	0.93	0.00	1.06		-0.95	2	
		33	10.0584	0.6096	218	78	-0.60	0.77	0.21	1.25		-0.80	2	
		34.2	10.42416	0.6096	212	90	-0.53	0.85	0.00	1.14		-0.87	2	
		37.2	11.33856	0.6096	235	80	-0.81	0.56	0.17	1.65		-0.61	2	
		40.4	12.31392	0.6096	145	70	0.54	0.77	0.34	1.35		-0.74	2	
										Total Fracture Density	1.352201952			

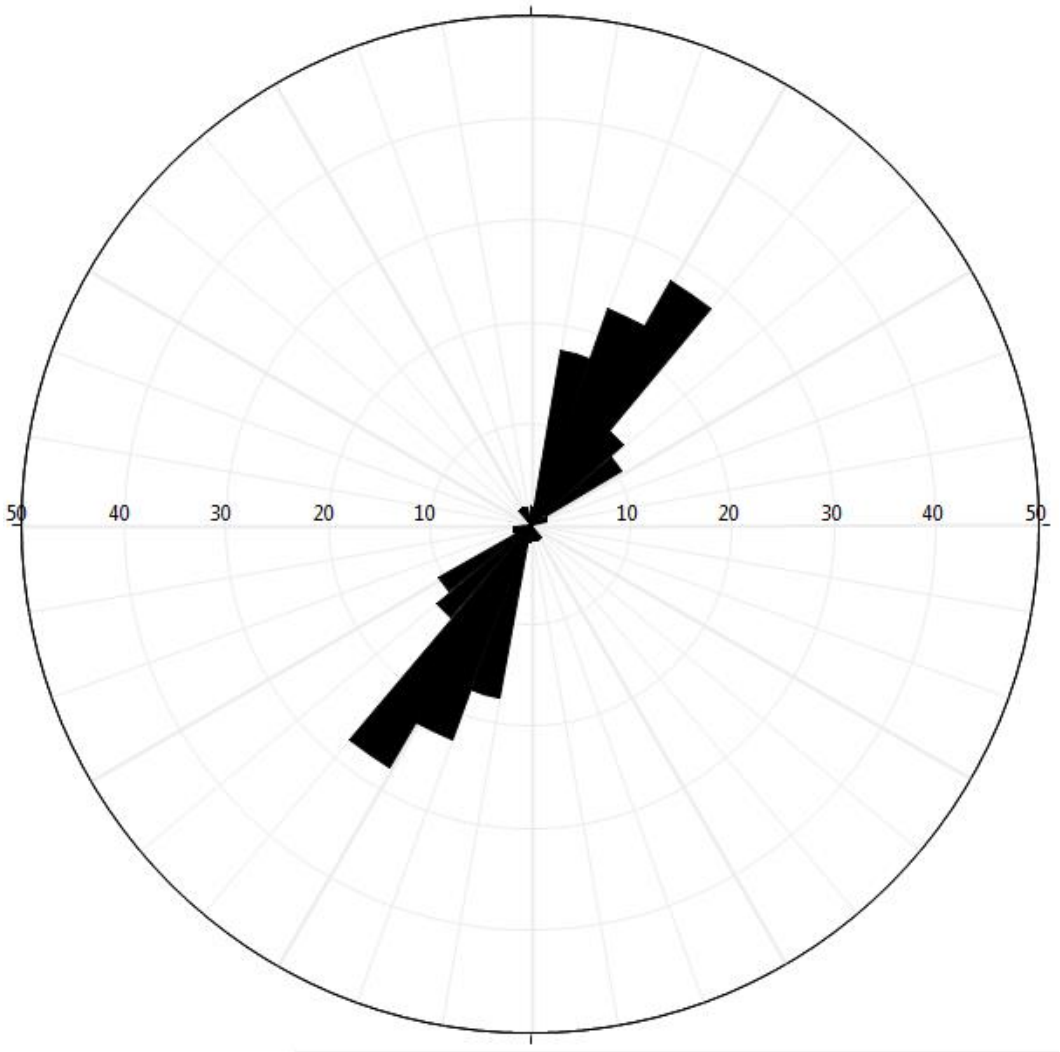

Figure 4-15. Rose Diagram of station 13-12-14-4 through 13-12-14-7, Atco Chalk

Figure 4-16. Boquillas Formation along Highway 90 outside of Del Rio, TX

Table 4-13. Boquillas Shale Data – 14-12-14-1 – Station 8

Station	UTM Coordinates	Strike of Outcrop (Right Hand Rule)	Dip of Outcrop (Right Hand Rule)	Thickness of Bed (M)	Strike of Bed (Right Hand Rule)	Dip of Bed (Right Hand Rule)	Trend of Scanline	Plunge of scanline	Length of Scanline	Scanline Vector x = North	Scanline Vector y = East	Scanline Vector z = down	Sample #	Sample strike (right hand rule)
14-12-14-1	14R 249046 E 3301336 N +/- 4m	285	77	0.762	285	0	285	0	14.0208	0.26	-0.97	0.00	14-12-14-1	N/A

Scan Line #	Trend	Fracture Distance (ft)	Fracture Distance (M)	Fracture Length (M)	Fracture Strike	Fracture Dip	Fracture Vector x coord	Fracture Vector y coord	Fracture Vector z coord	Weighting factor for fracture spacing		COS of angle between Scanline & Fracture Vector	Fracture Length (ft)	Additional Notes
1	285	1.3	0.39624	0.762	195	86	-0.26	0.96	0.07	1.00		-1.00	2.5	
		2.1	0.64008	0.762	214	90	-0.56	0.83	0.00	1.06		-0.95	2.5	
		3.6	1.09728	0.3048	167	90	0.22	0.97	0.00	1.13		-0.88	1	
		4.2	1.28016	0.3048	150	90	0.50	0.87	0.00	1.41		-0.71	1	
		5.7	1.73736	0.6096	160	89	0.34	0.94	0.02	1.22		-0.82	2	
		6.5	1.9812	0.762	211	90	-0.52	0.86	0.00	1.04		-0.96	2.5	
		8.6	2.62128	0.762	205	85	-0.42	0.90	0.09	1.02		-0.98	2.5	
		12	3.6576	0.762	153	69	0.42	0.83	0.36	1.44		-0.69	2.5	
		13.3	4.05384	0.762	199	86	-0.32	0.94	0.07	1.00		-1.00	2.5	
		13.6	4.14528	0.762	204	87	-0.41	0.91	0.05	1.01		-0.99	2.5	
		17.3	5.27304	0.762	178	87	0.03	1.00	0.05	1.05		-0.95	2.5	*Possible Borehole
		17.9	5.45592	0.762	177	90	0.05	1.00	0.00	1.05		-0.95	2.5	
		19.45	5.92836	0.6096	197	90	-0.29	0.96	0.00	1.00		-1.00	2	
		20.5	6.2484	0.762	203	90	-0.39	0.92	0.00	1.01		-0.99	2.5	
		20.95	6.38556	0.762	200	90	-0.34	0.94	0.00	1.00		-1.00	2.5	
		27.5	8.382	0.762	205	89	-0.42	0.91	0.02	1.02		-0.98	2.5	
		32.15	9.79932	0.762	199	89	-0.33	0.95	0.02	1.00		-1.00	2.5	
		33.8	10.30224	0.762	201	90	-0.36	0.93	0.00	1.01		-0.99	2.5	
		34.55	10.53084	0.6096	172	80	0.14	0.98	0.17	1.10		-0.91	2	
		42.1	12.83208	0.6096	180	89	0.00	1.00	0.02	1.04		-0.97	2	
		45.2	13.77696	0.6096	207	88	-0.45	0.89	0.03	1.02		-0.98	2	
										Total Fracture Density	1.615141125			

Table 4-14. Boquillas Shale Data – 14-12-14-2 – Station 9

Station	UTM Coordinates	Strike of Outcrop (Right Hand Rule)	Dip of Outcrop (Right Hand Rule)	Thickness of Bed (M)	Strike of Bed (Right Hand Rule)	Dip of Bed (Right Hand Rule)	Trend of Scanline	Plunge of scanline	Length of Scanline	Scanline Vector x = North	Scanline Vector y = East	Scanline Vector z = down	Sample #	Sample strike (right hand rule)
14-12-14-2	14R 249046 E 3301336 N +/- 4m	286	77	0.3048	285	0	286	8	15.24	0.27	-0.95	0.14	14-12-14-2	N/A

Scan Line #	Trend	Fracture Distance (ft)	Fracture Distance (M)	Fracture Length (M)	Fracture Strike	Fracture Dip	Fracture Vector x coord	Fracture Vector y coord	Fracture Vector z coord	Weighting factor for fracture spacing		COS of angle between Scanline & Fracture Vector	Fracture Length (ft)	Additional Notes
1	286	0.7	0.21336	0.1524	204	90	-0.41	0.91	0.00	1.02		-0.98	0.5	
		1.65	0.50292	0.1524	208	64	-0.42	0.79	0.44	1.24		-0.81	0.5	
		1.9	0.57912	0.3048	234	90	-0.81	0.59	0.00	1.28		-0.78	1	
		2.75	0.8382	0.3048	311	81	-0.75	-0.65	0.16	2.30		0.44	1	
		2.8	0.85344	0.3048	185	90	-0.09	1.00	0.00	1.03		-0.97	1	
		2.9	0.88392	0.3048	234	90	-0.81	0.59	0.00	1.28		-0.78	1	
		5.2	1.58496	0.3048	115	85	0.90	0.42	0.09	7.03		-0.14	1	
		5.3	1.61544	0.1524	225	75	-0.68	0.68	0.26	1.25		-0.80	0.5	
		5.8	1.76784	0.3048	234	80	-0.80	0.58	0.17	1.34		-0.74	1	
		7	2.1336	0.3048	152	82	0.46	0.87	0.14	1.46		-0.69	1	
		8.6	2.62128	0.1524	215	90	-0.57	0.82	0.00	1.07		-0.94	0.5	Rubble zone between 9 - 13.5 ft
		13	3.9624	0.3048	230	90	-0.77	0.64	0.00	1.22		-0.82	1	
		15.4	4.69392	0.3048	211	90	-0.52	0.86	0.00	1.05		-0.96	1	
		17	5.1816	0.3048	227	86	-0.73	0.68	0.07	1.19		-0.84	1	
		17.95	5.47116	0.3048	211	84	-0.51	0.85	0.10	1.07		-0.94	1	
		20.6	6.27888	0.3048	231	90	-0.78	0.63	0.00	1.23		-0.81	1	
		22.6	6.88848	0.3048	224	90	-0.69	0.72	0.00	1.14		-0.87	1	
		23.4	7.13232	0.3048	204	90	-0.41	0.91	0.00	1.02		-0.98	1	
		24.85	7.57428	0.3048	216	90	-0.59	0.81	0.00	1.07		-0.93	1	
		31.6	9.63168	0.3048	210	80	-0.49	0.85	0.17	1.08		-0.92	1	
		32.3	9.84504	0.3048	197	90	-0.29	0.96	0.00	1.01		-0.99	1	
		33.95	10.34796	0.3048	230	90	-0.77	0.64	0.00	1.22		-0.82	1	
		34.9	10.63752	0.3048	226	61	-0.63	0.61	0.48	1.46		-0.68	1	
		36.1	11.00328	0.3048	229	90	-0.75	0.66	0.00	1.20		-0.83	1	
		39.6	12.07008	0.3048	230	87	-0.76	0.64	0.05	1.23		-0.81	1	
		40.65	12.39012	0.3048	227	86	-0.73	0.68	0.07	1.19		-0.84	1	
		44.95	13.70076	0.3048	233	80	-0.79	0.59	0.17	1.33		-0.75	1	
		46.3	14.11224	0.3048	130	90	0.77	0.64	0.00	2.48		-0.40	1	
		48.05	14.64564	0.3048	235	81	-0.81	0.57	0.16	1.35		-0.74	1	
		48.75	14.859	0.3048	230	90	-0.77	0.64	0.00	1.22		-0.82	1	
		48.95	14.91996	0.3048	228	83	-0.74	0.66	0.12	1.22		-0.82	1	
		49.5	15.0876	0.3048	217	68	-0.56	0.74	0.37	1.24		-0.81	1	
										Total Fracture Density	2.972722846			

Table 4-15. Boquillas Shale Data – 14-12-14-3 – Station 10

Station	UTM Coordinates	Strike of Outcrop (Right Hand Rule)	Dip of Outcrop (Right Hand Rule)	Thickness of Bed (M)	Strike of Bed (Right Hand Rule)	Dip of Bed (Right Hand Rule)	Trend of Scanline	Plunge of scanline	Length of Scanline	Scanline Vector x = North	Scanline Vector y = East	Scanline Vector z = down	Sample #	Sample strike (right hand rule)
14-12-14-3	14R 257619 E 3300278 N +/- 5m	289	80	0.3048	289	0	289	5.5	15.24	0.32	-0.94	0.10	14-12-14-3	N/A

Scan Line #	Trend	Fracture Distance (ft)	Fracture Distance (M)	Fracture Length (M)	Fracture Strike	Fracture Dip	Fracture Vector x coord	Fracture Vector y coord	Fracture Vector z coord	Weighting factor for fracture spacing		COS of angle between Scanline & Fracture Vector	Fracture Length (ft)	Additional Notes
1	289	0.5	0.1524	0.3048	225	90	-0.71	0.71	0.00	1.12		-0.89	1	
		1.6	0.48768	0.3048	238	86	-0.85	0.53	0.07	1.31		-0.76	1	
		2.2	0.67056	0.3048	230	90	-0.77	0.64	0.00	1.17		-0.85	1	
		2.75	0.8382	0.3048	217	90	-0.60	0.80	0.00	1.06		-0.95	1	
		3.4	1.03632	0.3048	245	89	-0.91	0.42	0.02	1.45		-0.69	1	
		5.15	1.56972	0.3048	235	87	-0.82	0.57	0.05	1.25		-0.80	1	
		6.8	2.07264	0.3048	242	74	-0.85	0.45	0.28	1.49		-0.67	1	
		8.5	2.5908	0.3048	241	90	-0.87	0.48	0.00	1.35		-0.74	1	
		9.2	2.80416	0.3048	247	82	-0.91	0.39	0.14	1.55		-0.65	1	
		10.3	3.13944	0.3048	241	90	-0.87	0.48	0.00	1.35		-0.74	1	
		10.8	3.29184	0.3048	236	87	-0.83	0.56	0.05	1.27		-0.79	1	
		11.2	3.41376	0.3048	245	90	-0.91	0.42	0.00	1.45		-0.69	1	
		13.8	4.20624	0.3048	233	89	-0.80	0.60	0.02	1.21		-0.82	1	
		16.2	4.93776	0.3048	240	84	-0.86	0.50	0.10	1.36		-0.74	1	17 to 27 ft - covered
		28	8.5344	0.3048	237	90	-0.84	0.54	0.00	1.27		-0.78	1	
		28.85	8.79348	0.3048	234	90	-0.81	0.59	0.00	1.23		-0.82	1	
		31	9.4488	0.3048	238	85	-0.84	0.53	0.09	1.31		-0.76	1	
		33.3	10.14984	0.3048	236	90	-0.83	0.56	0.00	1.26		-0.79	1	
		35.2	10.72896	0.3048	238	87	-0.85	0.53	0.05	1.30		-0.77	1	
		36.3	11.06424	0.3048	228	90	-0.74	0.67	0.00	1.15		-0.87	1	
		38.35	11.68908	0.3048	239	87	-0.86	0.51	0.05	1.32		-0.76	1	
		39.7	12.10056	0.3048	243	87	-0.89	0.45	0.05	1.41		-0.71	1	
		40.7	12.40536	0.3048	240	85	-0.86	0.50	0.09	1.35		-0.74	1	
		42.4	12.92352	0.3048	239	84	-0.85	0.51	0.10	1.34		-0.75	1	
		43.2	13.16736	0.3048	240	71	-0.82	0.47	0.33	1.47		-0.68	1	
		43.1	13.13688	0.3048	218	90	-0.62	0.79	0.00	1.06		-0.94	1	
		45.25	13.7922	0.3048	238	89	-0.85	0.53	0.02	1.30		-0.77	1	
		45.63	13.908024	0.3048	220	90	-0.64	0.77	0.00	1.08		-0.93	1	
		48	14.6304	0.3048	237	90	-0.84	0.54	0.00	1.27		-0.78	1	
		48.9	14.90472	0.3048	227	90	-0.73	0.68	0.00	1.14		-0.88	1	
										Total Fracture Density	2.535168212			

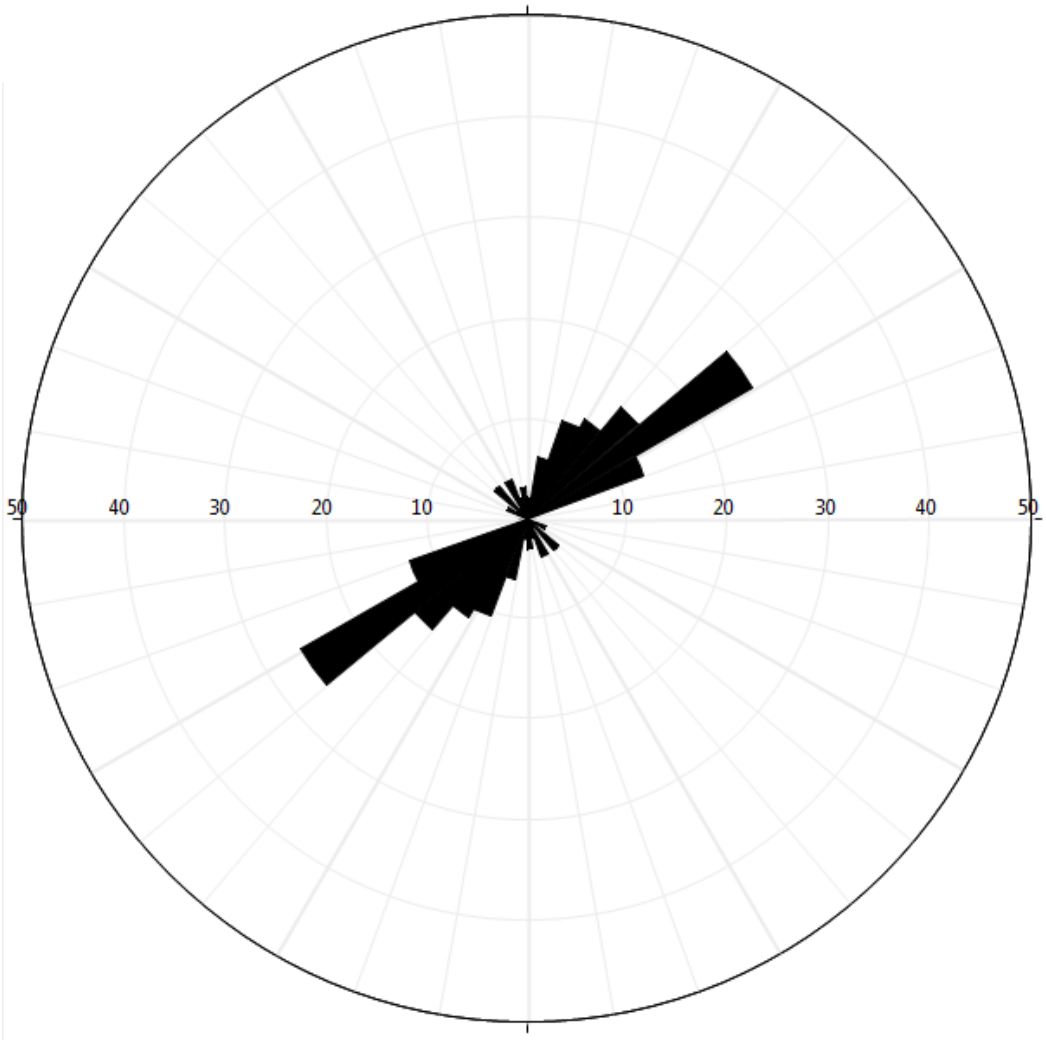

Figure 4-17. Rose Diagram of stations 13-12-14-3 and 14-12-14-1 through 14-12-14-3 - Boquillas Shale

Table 4-16. Del Rio Formation Data – 14-12-14-4 – Station 11

Station	UTM Coordinates	Strike of Outcrop (Right Hand Rule)	Dip of Outcrop (Right Hand Rule)	Thickness of Bed (M)	Strike of Bed (Right Hand Rule)	Dip of Bed (Right Hand Rule)	Trend of Scanline	Plunge of scanline	Length of Scanline	Scanline Vector x = North	Scanline Vector y = East	Scanline Vector z = down	Sample #	Sample strike (right hand rule)
14-12-14-4	14R 269356 E 3295561 N +/- 3m	180	90	0.3048	180	0	180	0	13.716	-1.00	0.00	0.00	14-12-14-4	N/A

Scan Line #	Trend	Fracture Distance (ft)	Fracture Distance (M)	Fracture Length (M)	Fracture Strike	Fracture Dip	Fracture Vector x coord	Fracture Vector y coord	Fracture Vector z coord	Weighting factor for fracture spacing		COS of angle between Scanline & Fracture Vector	Fracture Length (ft)	Additional Notes
1	180	1.4	0.42672	0.3048	105	90	0.97	0.26	0.00	1.04		-0.97	1	
		5.3	1.61544	0.3048	74	90	0.96	-0.28	0.00	1.04		-0.96	1	
		5.5	1.6764	0.3048	86	90	1.00	-0.07	0.00	1.00		-1.00	1	
		6.6	2.01168	0.3048	56	88	0.83	-0.56	0.03	1.21		-0.83	1	
		8.1	2.46888	0.3048	102	80	0.96	0.20	0.17	1.04		-0.96	1	
		12	3.6576	0.3048	102	90	0.98	0.21	0.00	1.02		-0.98	1	
		14.35	4.37388	0.3048	101	86	0.98	0.19	0.07	1.02		-0.98	1	
		14.85	4.52628	0.3048	125	84	0.81	0.57	0.10	1.23		-0.81	1	
		17	5.1816	0.1524	66	90	0.91	-0.41	0.00	1.09		-0.91	0.5	
		17.5	5.334	0.3048	130	84	0.76	0.64	0.10	1.31		-0.76	1	
		18.5	5.6388	0.1524	80	90	0.98	-0.17	0.00	1.02		-0.98	0.5	
		20.8	6.33984	0.1524	114	88	0.91	0.41	0.03	1.10		-0.91	0.5	
		22.6	6.88848	0.3048	141	84	0.63	0.77	0.10	1.60		-0.63	1	
		25.5	7.7724	0.3048	90	90	1.00	0.00	0.00	1.00		-1.00	1	
		26.7	8.13816	0.3048	42	90	0.67	-0.74	0.00	1.49		-0.67	1	
		30.3	9.23544	0.3048	100	86	0.98	0.17	0.07	1.02		-0.98	1	
		33.3	10.14984	0.3048	117	86	0.89	0.45	0.07	1.13		-0.89	1	
		34.7	10.57656	0.3048	41	90	0.66	-0.75	0.00	1.52		-0.66	1	
		41.3	12.58824	0.3048	82	80	0.98	-0.14	0.17	1.03		-0.98	1	
		42.5	12.954	0.3048	94	85	0.99	0.07	0.09	1.01		-0.99	1	
		45	13.716	0.3048	105	86	0.96	0.26	0.07	1.04		-0.96	1	
										Total Fracture Density	1.745482855			

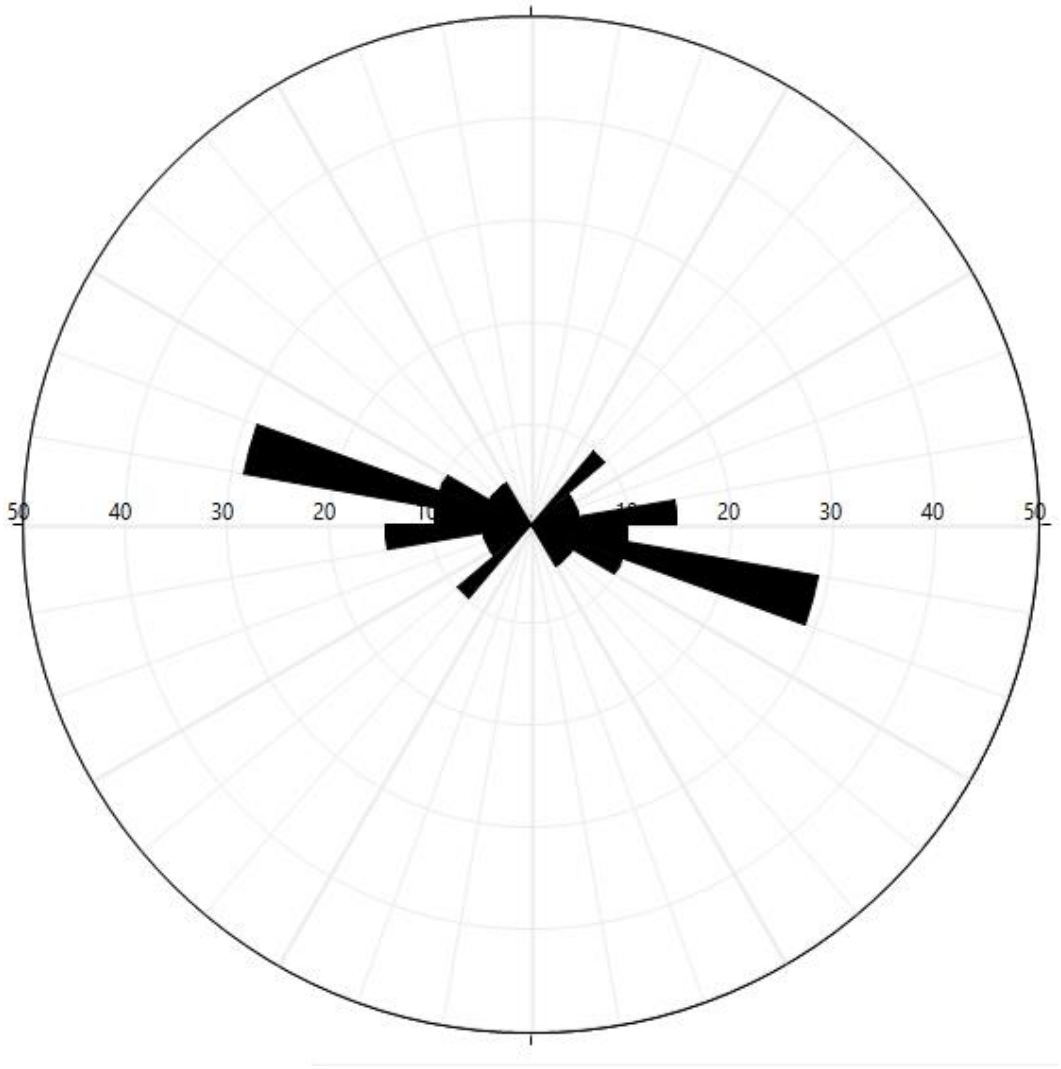

Figure 4-18. Rose Diagram of station 14-12-14-4, Del Rio Formation

Table 4-17. Salmon Peak Limestone Data – 14-12-14-5 – Station 12

Station	UTM Coordinates	Strike of Outcrop (Right Hand Rule)	Dip of Outcrop (Right Hand Rule)	Thickness of Bed (M)	Strike of Bed (Right Hand Rule)	Dip of Bed (Right Hand Rule)	Trend of Scanline	Plunge of scanline	Length of Scanline	Scanline Vector x = North	Scanline Vector y = East	Scanline Vector z = down	Sample #	Sample strike (right hand rule)
14-12-14-5	14R 304695 E 3270077 N +/- 4m	145	4	1.2192	145	0	145	0	10.668	-0.82	0.57	0.00	14-12-14-5	N/A

Scan Line #	Trend	Fracture Distance (ft)	Fracture Distance (M)	Fracture Length (M)	Fracture Strike	Fracture Dip	Fracture Vector x coord	Fracture Vector y coord	Fracture Vector z coord	Weighting factor for fracture spacing		COS of angle between Scanline & Fracture Vector	Fracture Length (ft)	Additional Notes
1	145	2.3	0.70104	2.1336	50	90	0.77	-0.64	0.00	1.00		-1.00	7	
		3.9	1.18872	1.6764	53	90	0.80	-0.60	0.00	1.00		-1.00	5.5	
		5.3	1.61544	1.2192	55	90	0.82	-0.57	0.00	1.00		-1.00	4	
		6.4	1.95072	1.0668	60	90	0.87	-0.50	0.00	1.00		-1.00	3.5	
		7.1	2.16408	0.9144	55	90	0.82	-0.57	0.00	1.00		-1.00	3	
		7.9	2.40792	2.4384	57	90	0.84	-0.54	0.00	1.00		-1.00	8	
		9.9	3.01752	1.524	57	90	0.84	-0.54	0.00	1.00		-1.00	5	
		11.3	3.44424	1.2192	50	90	0.77	-0.64	0.00	1.00		-1.00	4	
		14.05	4.28244	2.286	45	90	0.71	-0.71	0.00	1.02		-0.98	7.5	
		17.45	5.31876	0.9144	54	90	0.81	-0.59	0.00	1.00		-1.00	3	
		23.6	7.19328	3.048	55	90	0.82	-0.57	0.00	1.00		-1.00	10	
		26.1	7.95528	1.8288	60	90	0.87	-0.50	0.00	1.00		-1.00	6	
		27.1	8.26008	2.1336	41	90	0.66	-0.75	0.00	1.03		-0.97	7	
		28.2	8.59536	1.524	58	90	0.85	-0.53	0.00	1.00		-1.00	5	
		30.25	9.2202	1.8288	56	90	0.83	-0.56	0.00	1.00		-1.00	6	
		32.7	9.96696	2.4384	57	85	0.84	-0.54	0.09	1.00		-1.00	8	
										Total Fracture Density	1.50630455			

4.2 Lab Measurements

The elastic moduli, bulk density, and porosity of each rock sample were measured using UTA laboratory procedures. The mineralogical percentages used for estimating the brittleness index were obtained by ALS Empirica, a petroleum industry service company, using their own X-Ray Diffraction technology.

4.2.1 Elastic Rock Properties

The elastic shear modulus, Poisson's ratio and bulk density of each sample were measured in order to use Equations 13 and 14. These material properties were estimated using a combination of acoustic wave velocities (p and s-wave) along with bulk density data from mercury intrusion porosimetry, as described by Webb (2001). Rock preparation consisted of cutting the samples perpendicular to bedding utilizing a diamond saw. Acoustic velocity measurements were made by using a PC oscilloscope (PicoScope 5023), an ultrasonic pulsar/receiver (Model 5077 PR, Olympus), and an ultrasonic transducer (V101 – RB and V150 – RB, Olympus for P and S – Wave velocities). Acoustic testing was done in Dr. Xinbao Yu's engineering lab at UTA. The transducer and receiver were attached to the opposing parallel surfaces in order to measure the p and s-wave transit time in microseconds. The velocities were calculated by dividing the sample length by the measured transit time.

Figure 4-19. Preparing samples for acoustic testing using the Water Saw in the UTA Geology Thin Section Lab

Figure 4-20. Example of samples cut with smooth, parallel surfaces perpendicular to bedding in order to optimize acoustic velocity measurements

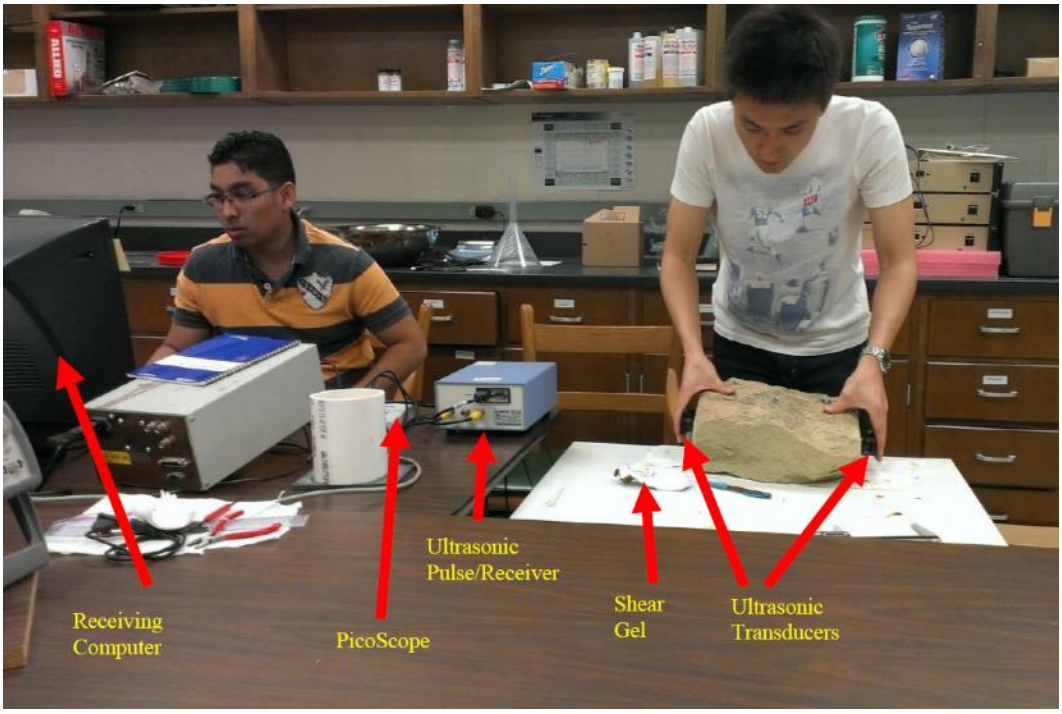

Figure 4-21. ATSM 2845 equipment used for acoustic wave velocity analysis; Image taken from Zastoupil (2015)

Figure 4-22. Measuring acoustic wave velocities using the ATSM 2845

Table 4-18. Acoustic Velocity results. Sample 14-12-14-2B, highlighted in yellow, was too small to analyze

Station	**Lithology**	**Length (mm)**	**Vp (usec)**	**Vs (usec)**	**Vp (ft/sec)**	**Vs (ft/sec)**
PD STA 1	Sandstone	173	64.51	98.52	8798.609502	5761.153263
PD STA 2	Sandstone	259	83.45	124.59	10182.62911	6820.440252
PD STA 3	Siltstone	174	26.80	47.09	21297.22222	12121.73913
BH STA-1	Dolomite	165	20.66	41.73	26232.06196	12987.16511
BH STA-2	Dolomite	181	23.56	50.43	22135.71961	11772.35772
13-12-14-1	Limestone	212.3	18.3	39.72	38061.3284	17535.8084
13-12-14-2	Limestone	136.1	18.6	44.6	24006.57579	10011.71098
13-12-14-3A	Shale	201.7	27.16	48.13	24364.7057	13749.12543
13-12-14-3B	Shale	161.44	28.31	53.59	18709.24736	9883.537836
13-12-14-4	Chalk	164.4	13.18	24.16	40923.37471	22324.92048
13-12-14-5	Chalk	170.2	10.3	24.37	54213.4903	22913.37506
13-12-14-6	Chalk	91.22	10.5	24.37	28502.68716	12280.59972
13-12-14-7	Chalk	173.4	12.7	21.41	44795.08959	26571.58514
14-12-14-1A	Shale	146.9	23.45	49.35	20552.46825	9766.066476
14-12-14-1B	Shale	178.8	29.71	56.54	19744.67093	10375.20646
14-12-14-2A	Shale	105.25	10.91	27.23	31650.63235	12681.17514
14-12-14-2B	Shale	N/A	N/A	N/A	N/A	N/A
14-12-14-3A	Shale	128.2	26.24	54.09	16029.10345	7775.996941
14-12-14-3B	Shale	117.7	25.8	46.25	14967.24247	8349.294176
14-12-14-4	Clay	153	28.31	51.37	17731.13755	9771.627486
14-12-14-5	Limestone	141.5	14.94	31.62	31073.55055	14681.81041

4.2.2 Mercury Injection

Bulk density was measured utilizing mercury intrusion porosimetry. Smaller fragments of each rock sample were cut into centimeter size cubes for testing. Mercury is a non-wetting liquid that must be forced into pores by application of external pressure (Webb, 2001). By surrounding each cube with liquid mercury and applying pressure, mercury begins to enter the sample pores. With greater pressures, the rate of mercury saturation increases. During the sample analysis, applied pressure and intrusion volume at the specified pressure is measured. The volume of mercury displaced at the minimum pressure and that displaced at maximum pressure are used to determine bulk density and skeletal density using the volumetric equations below (Webb, 2001; Gao and Hu, 2013):

$$V_{Bulk} = V_{solid} + V_{Open\ Pores} + V_{Closed\ Pores} + V_{Internal\ Voids} + V_{External\ Voids}$$

and

$$V_{Skeleton} = V_{solid} + V_{Closed\ Pores}$$

With the acquired sonic and bulk density values, the elastic properties were estimated using the following equations:

$$\mu = V_s^{\,2}\rho \qquad \text{Eq. 16}$$

and

$$v = \frac{(\frac{V_p}{V_s})^2}{2[(\frac{V_p}{V_s})^2 - 1]} \qquad \text{Eq. 17}$$

Figure 4-23. Sample preparation for Mercury Intrusion Porosimetry. Samples were cut in 3x3x3 cubes for testing

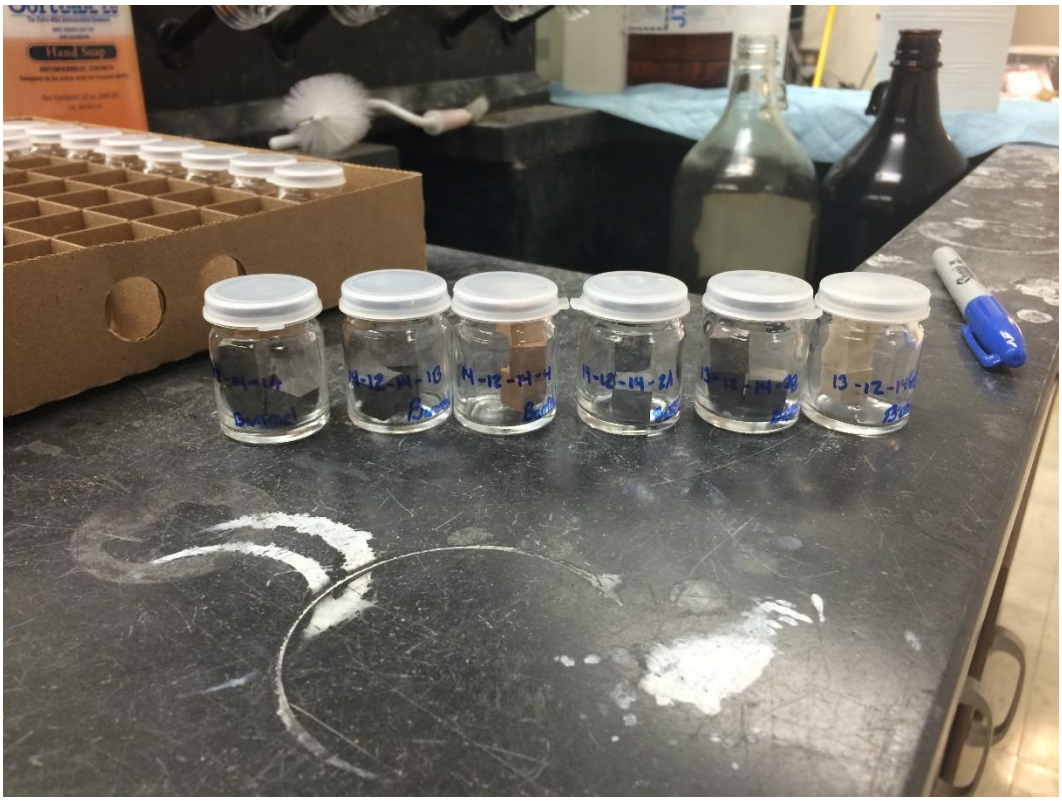

Figure 4-24. Lineup of six Del Rio samples awaiting mercury intrusion analysis

Figure 4-25. AutoPore IV 9510 used for the Mercury Intrusion Analysis; Image taken from Zastoupil (2015)

Table 4-19. Results from the Mercury Intrusion Porosimetry analysis

Station	Lithology	Density Dry (gm/cc)	Porosity (%)
PD STA 1	Sandstone	1.835	30.58
PD STA 2	Sandstone	1.945	26.46
PD STA 3	Siltstone	1.258	7.060
BH STA 1	Dolomite	2.417	11.23
BH STA 2	Dolomite	2.403	12.94
13-12-14-1	Limestone	2.486	5.675
13-12-14-2	Limestone	2.562	0.410
13-12-14-3	Shale	2.218	8.673
13-12-14-4	Chalk	2.538	8.350
13-12-14-5	Chalk	2.426	8.182
13-12-14-6	Chalk	2.489	7.872
13-12-14-7	Chalk	2.488	8.027
14-12-14-1	Shale	2.498	0.591
14-12-14-2	Shale	2.438	0.562
14-12-14-3	Shale	2.145	0.803
14-12-14-4	Clay	2.359	12.93
14-12-14-5	Limestone	2.512	7.810

Station	Lithology	Density Dry (gm/cc)	Porosity (%)
PD STA 1	Sandstone	1.835	30.58
PD STA 2	Sandstone	1.945	26.46
PD STA 3	Siltstone	1.258	7.060
BH STA 1	Dolomite	2.417	11.23
BH STA 2	Dolomite	2.403	12.94
13-12-14-1	Limestone	2.486	5.675
13-12-14-2	Limestone	2.562	0.410
13-12-14-3	Shale	2.218	8.673
13-12-14-4	Chalk	2.538	8.350
13-12-14-5	Chalk	2.426	8.182
13-12-14-6	Chalk	2.489	7.872
13-12-14-7	Chalk	2.488	8.027
14-12-14-1	Shale	2.498	0.591
14-12-14-2	Shale	2.438	0.562

14-12-14-3	Shale	2.145	0.803
14-12-14-4	Clay	2.359	12.925
14-12-14-5	Limestone	2.512	7.810

4.2.3 X-Ray Diffraction

While estimating geomechanical brittleness utilizes elastic parameters derived from field measurements and physical analysis, the brittleness index (BI) uses estimates based on mineralogical content. To help support the project, ALS Empirica performed the X-Ray Diffraction (XRD) Bulk Mineral Analysis without charge. The process is done by measuring the interaction of the XRD incident rays with the rock minerals, producing constructive interference and a diffracted ray that exits the sample at an angle Φ, measured from the incident ray. The angle Φ depends on the spacing of atomic layers in the crystal structure (Dutrow and Clark, 2015). The d-spacings are used to identify each mineral present in the sample.

The data from ALS was used in Equation 1 and Equation 2 to calculate the Brittleness Index. The results from their procedures along with the brittleness index are found in Table 21 below.

Table 4-20. Mineral content (in percentages) and Brittleness Index for each sample;

Analysis performed by ALS Empirica Oil and Gas

Mineral Content and Brittleness Index					
Station	Total Clay	Qz + Fsp	Total Carb	TOC	Brittleness Index
13-12-14-1	8.007	5.423	86.348	0.222	0.918
13-12-14-2	11.223	3.360	85.153	0.265	0.885
13-12-14-3A	15.764	26.123	52.655	5.458	0.788
13-12-14-3B	17.378	19.124	59.427	4.071	0.786
13-12-14-5	26.370	2.860	70.558	0.212	0.734
13-12-14-6	23.486	5.034	71.326	0.154	0.764
13-12-14-7	16.444	4.369	78.995	0.192	0.834
14-12-14-1A	17.608	23.622	55.181	3.590	0.788
14-12-14-1B	16.208	23.111	56.421	4.260	0.795
14-12-14-2A	23.678	18.418	56.367	1.538	0.748
14-12-14-2B	32.182	19.614	47.081	1.123	0.667
14-12-14-3A	18.799	17.236	63.843	0.122	0.811
14-12-14-3B	22.671	14.117	63.070	0.142	0.772
14-12-14-4	20.809	58.750	18.710	1.732	0.775
14-12-14-5	17.625	4.610	77.582	0.183	0.822
PD STA 1	36.604	50.352	12.861	0.183	0.632
PD STA 2	31.749	38.396	29.663	0.191	0.681
PD STA 3	38.665	48.897	12.020	0.418	0.609
BH STA 1	14.357	1.771	83.604	0.267	0.854
BH STA 2	12.764	9.157	77.753	0.327	0.869

Chapter 5

Results

There have been numerous efforts to define and measure brittleness over the years (Hucka and Das, 1974; Becker et al, 1984; Kahraman, 2002; and others). Wickham et al (2013) defined brittleness in terms of a geomechanical equation for fracture density (Equation 13).

Equation 13 can be written in its dimensionless form (Equation 14 and below) where it is linear if the strain invariants A and B are constant. If measurements are made on multiple layers all with the same strain state, they should plot as a straight line using Equation 14 as long as the layers had not failed in tension.

$$\frac{F_d K_{Ic}^2}{4\mu^2(1+v)} = A\frac{v}{1-2v} + B$$

The fracture density and material property measurements from nearby localities were all plotted using Equation 14 to see if the layers were subjected to the same strain state or were deformed beyond their tensile strength, leading to overlapping stress shadows prohibiting further joint development.

In addition, the relative geomechanical brittleness of each measured layer in all the localities can be calculated using Equation 13 shown below assuming they were all subjected to the same uniaxial extension. In other words, layers with higher fracture density are more brittle than layers with lower fracture density if they were all subjected to the same uniaxial extension.

$$\boldsymbol{F_d} = \frac{4\mu^2(1+v)}{K^2{}_{Ic}}\left(A\frac{v}{1-2v} + B\right)$$

Finally, the relative brittleness based on the geomechanical equation for fracture density was compared with the Brittleness Index based on mineralogy (Equation 2 and below). A geomechanical definition of brittleness would be better than one based on mineralogy, but the mineralogy brittleness index may be a good proxy because the material properties of the geomechanical brittleness depend on mineralogy. In addition, the Geomechanical Brittleness is also influenced by porosity while the mineralogical definition is not. The mineralogical brittleness Index were compared with the Geomechanical Brittleness to see how well they coincide.

$$BI = \frac{Qz + Dol}{Qz + Dol + Limestone + Cl + TOC}$$

5.1 Results: Palo Duro Canyon, TX

Figure 5-1 displays the results for Equation 14. The data yields a relatively high r^2 of 0.9701 and a positive slope of 78.45, indicating that the samples were subjected to equal strain states. However, because there are only three points and two of them plot close together, the linear relationship may not be that significant.

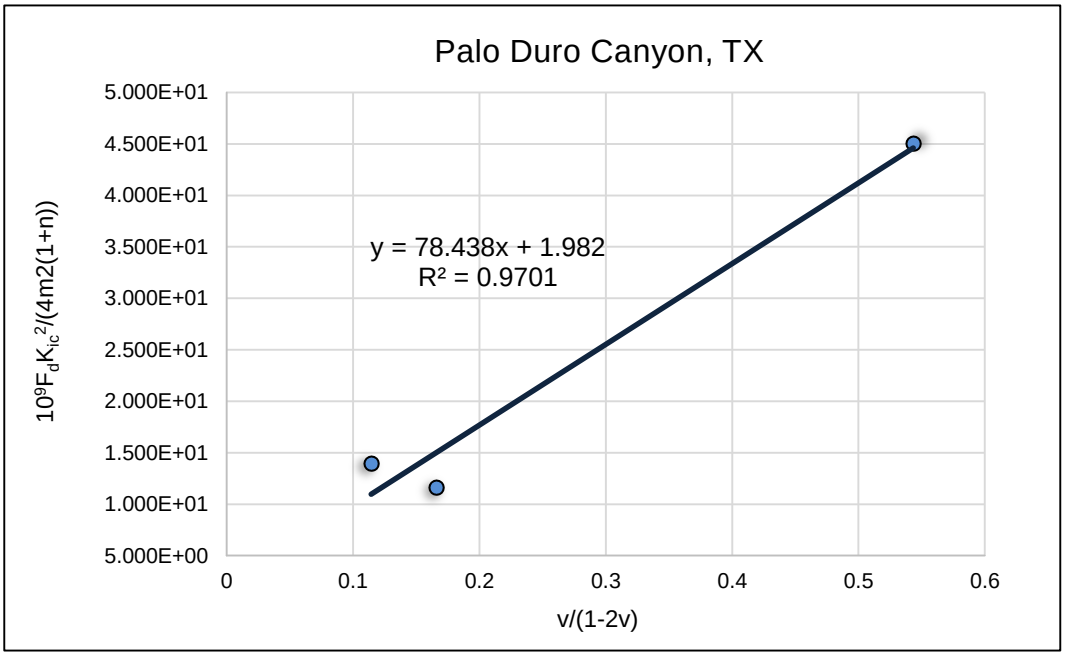

Figure 5-1. Plot of Equation 14 – Palo Duro Canyon, TX

Using Equation 13, each sample was graphed in terms of their uniaxial extensional strain state to calculate Geomechanical Brittleness shown by the fracture density (Figure 5-2). Using the criteria of equal uniaxial strain conditions, the rock with higher fracture density is more brittle than those with lower fracture density. For

example, at a uniaxial strain of 1.2 x 10^{-4}, specimen PD STA-2 is more than 1.7 times more brittle than sample PD STA-3.

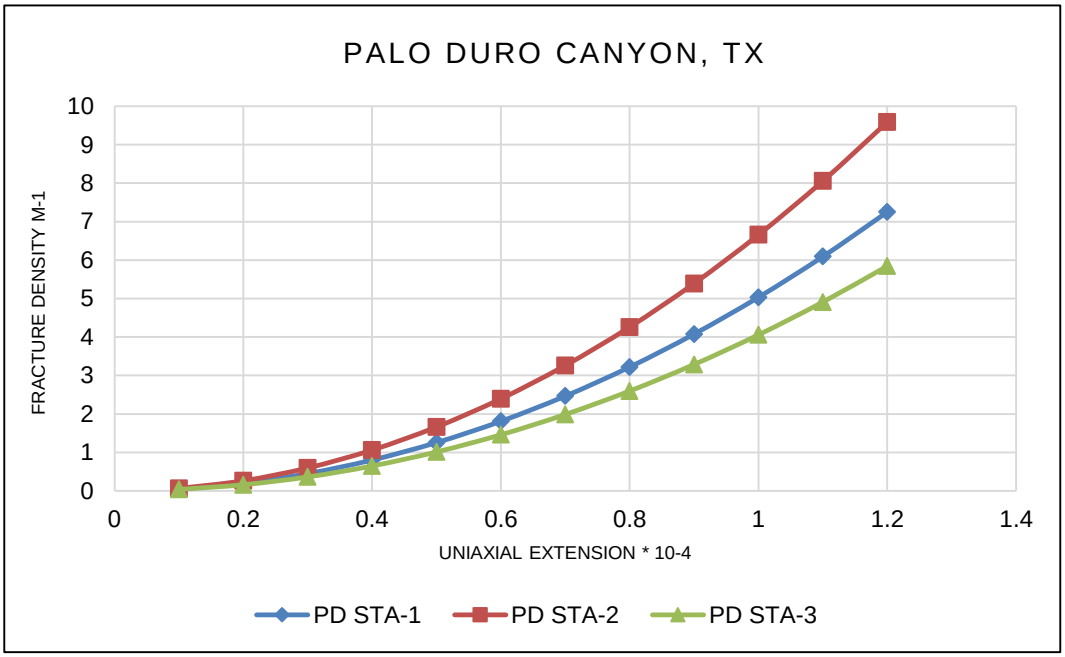

Figure 5-2. Comparative Brittleness Plot - Uniaxial Extension vs. Fracture Density; Palo Duro Canyon, TX

A comparison of calculated fracture density and the XRD brittleness index is shown below in Table 23. The results directly correlate with the Brittleness Index, where PD STA-3 shows the lowest mineralogical brittleness and the lowest geomechanical brittleness. Likewise, PD STA-2 shows the highest geomechanical brittleness and the highest mineralogical brittleness.

Table 5-1. Comparison of XRD Brittleness Index values with the Calculated Fracture Density for samples from Palo Duro Canyon, TX

Station	Geomechanical Brittleness	Mineralogical Brittleness (%)
PD STA 3	5.845014073	61
PD STA 1	7.253615423	63
PD STA 2	9.591123737	68

Plotting the Geomechanical Brittleness versus the Mineralogical Brittleness (Figure 5-3) yields a positive correlation of 0.99.

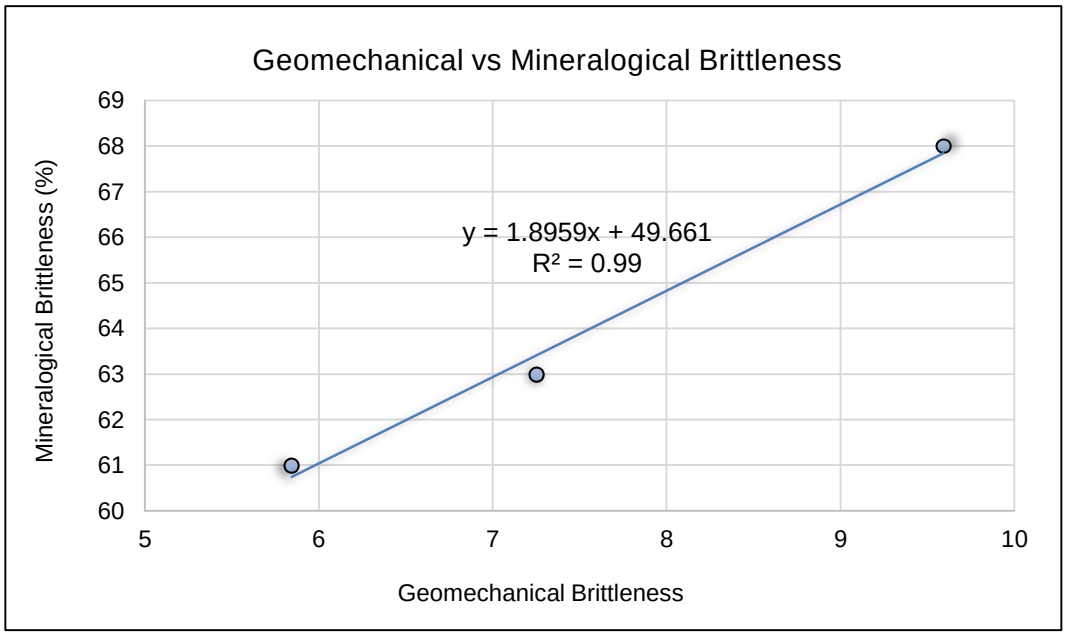

Figure 5-3. Correlation of the Geomechanical Brittleness versus the Mineralogical Brittleness – Palo Duro Canyon, TX

5.2 Results: Bighorn Basin, WY

Figure 5-4 displays the results for Equation 14. The data yields a negative slope of -29.75, indicating that the samples were either subjected to different strain states or deformed beyond their tensile strength. Note that with only two samples from the area, the data is incomplete and more sampling is needed to obtain meaningful results.

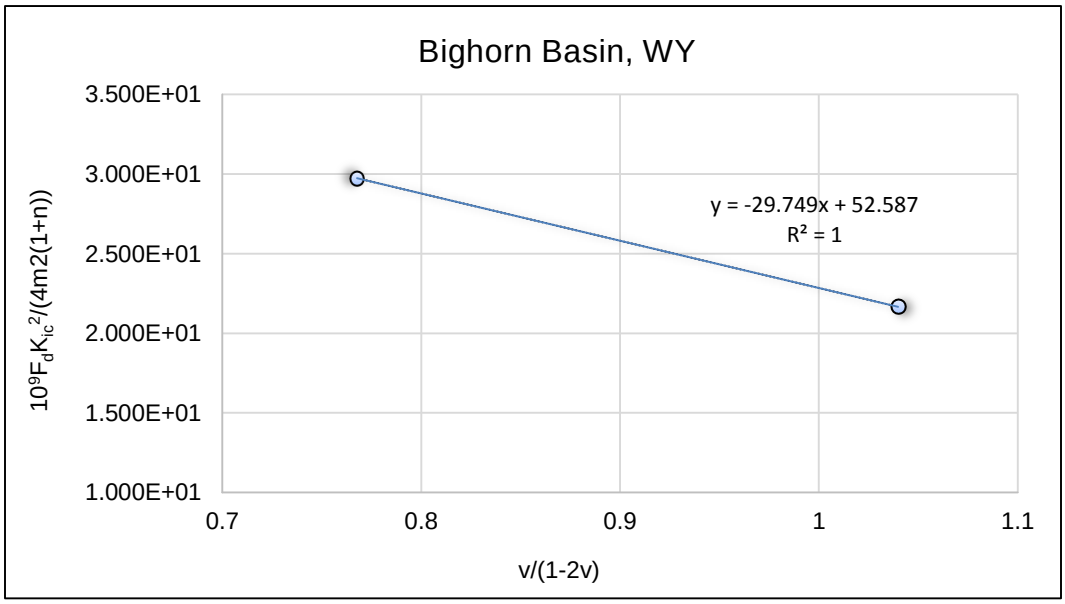

Figure 5-4. Plot of Equation 14 – Bighorn Basin, WY

The Geomechanical brittleness of the Bighorn Basin specimens is shown in Figure 5-5. At a uniaxial strain of 1.2×10^{-4}, specimen BH STA-1 is almost 1.5 times more brittle than BH STA-2.

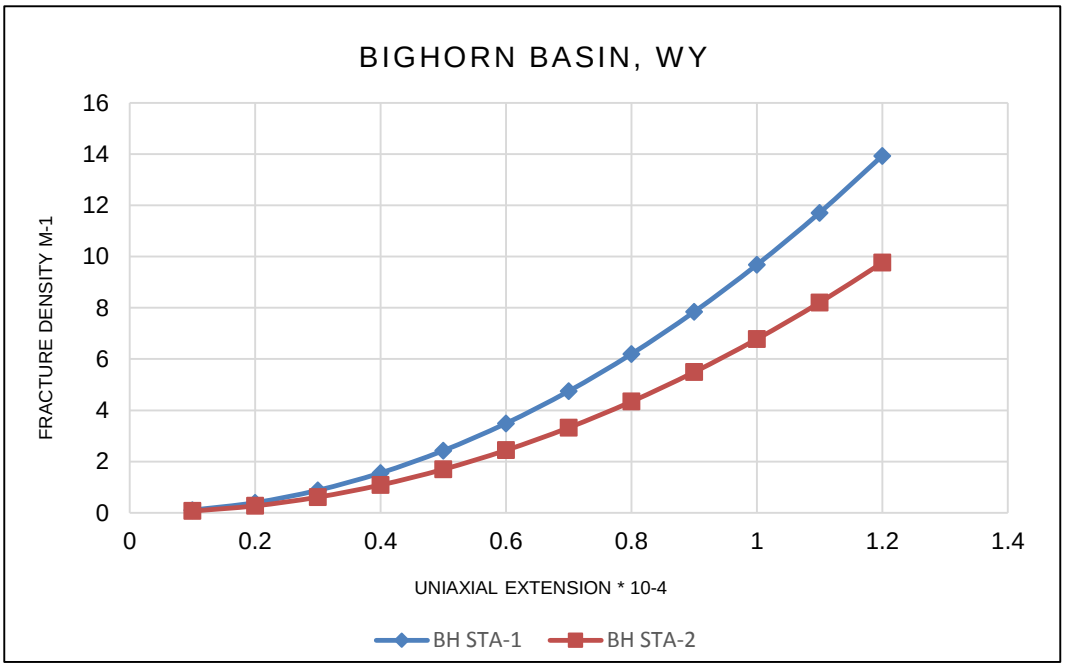

Figure 5-5. Comparative Brittleness Plot - Uniaxial Extension vs. Fracture Density; Bighorn Basin, WY

The Geomechanical brittleness disagrees with the mineralogical brittleness (Table 24). BH STA-1 has the greatest geomechanical brittleness, but the least mineralogical brittleness.

Table 5-2. Comparison of XRD Brittleness Index with the calculated Fracture Density for samples from Bighorn Basin, WY

Station	Geomechanical Brittleness	Mineralogical Brittleness (%)
BH STA-1	13.93180917	85
BH STA-2	9.764205349	87

Plotting the Geomechanical Brittleness versus the Mineralogical Brittleness (Figure 5-6) for the Bighorn samples yields a correlation of 1 due to only two data points.

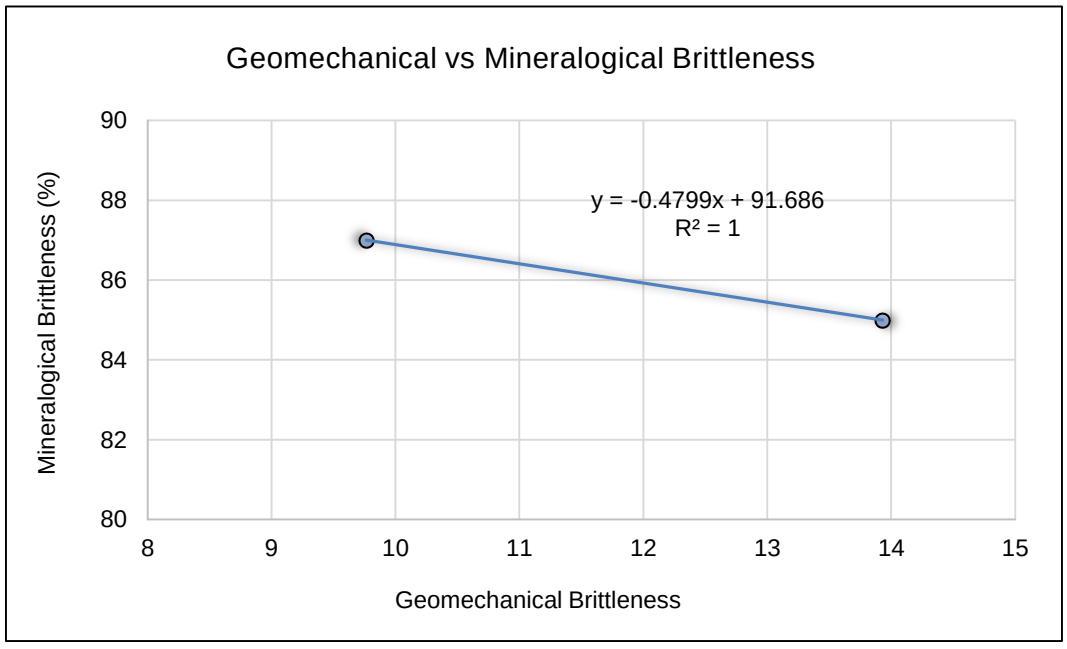

Figure 5-6. Correlation of the Geomechanical Brittleness versus the Mineralogical Brittleness – Bighorn Basin, WY

5.3 Results: Highway 90 – Del Rio, TX

Figure 5-7 displays the results for dimensionless Equation 14. The data yields an r2 value of 0.0005 and plot as a slightly positive slope of 0.3318, indicating that the samples were subjected to different strain states or exceeded their tensile strength. The fact that the joint orientations were quite different from sample to sample (Figures 4-8, 4-10, 4-15, 4-17, 4-18) suggests that the strains were significantly different as well.

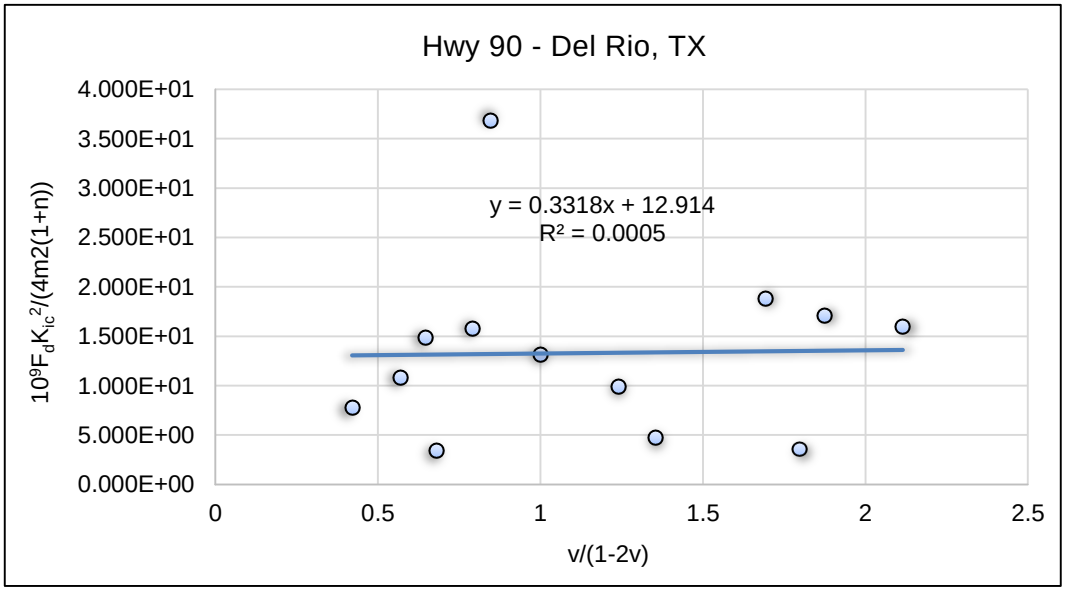

Figure 5-7. Plot of Equation 14 – Del Rio, TX

Figure 5-8 shows that at a uniaxial strain of 1.2×10^{-4}, sample 13-12-14-1 has a significantly greater geomechanical brittleness than the other samples (over 60). Sample 14-12-14-3 is the least brittle with a Geomechanical Brittleness of 11.72.

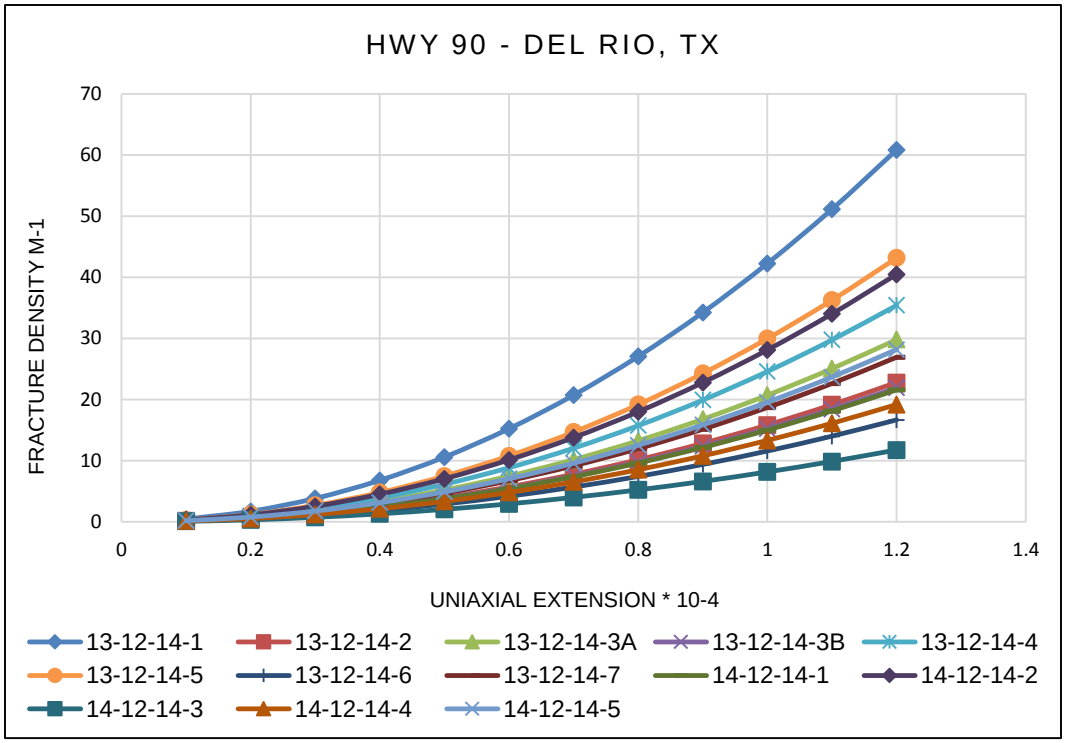

Figure 5-8. Comparative Brittleness Plot - Uniaxial Extension vs. Fracture Density; Del Rio, TX

Comparison of the Mineralogical Brittleness index with the Geomechanical brittleness (Table 25) shows little agreement. In Table 25, the order the Geomechanical and Mineralogical brittleness is shown in parentheses. The closest agreement is between specimens 14-12-14-5 and 13-12-14-3A, but the others lack any significant correlation. This is confirmed by graphing the Geomechanical Brittleness versus the Mineralogical Brittleness (Figure 5-9) which has a very low correlation coefficient of 0.0512.

Table 5-3. Comparison of Mineralogical Brittleness Index percentages with the calculated Geomechanical Brittleness for the Del Rio, TX samples. The Geomechanical Brittleness is arranged from smallest to largest with the order shown in parentheses. The mineralogical brittleness in table 5-3 is shown for the same samples with the brittleness order also shown in parentheses.

Station	Geomechanical Brittleness	Mineralogical Brittleness (%)
14-12-14-3	11.72132292 (13)	79 (5)
13-12-14-6	16.65424908 (12)	76 (8)
14-12-14-4	19.15687905 (11)	77 (7)
14-12-14-1	21.56403939 (10)	79 (5)
13-12-14-3B	21.92459851 (9)	79 (5)
13-12-14-2	22.76954564 (8)	89 (2)
13-12-14-7	26.9157351 (7)	83 (3)
14-12-14-5	28.15947616 (6)	82 (4)
13-12-14-3A	29.82868725 (5)	79 (5)
13-12-14-4	35.42464052 (4)	78 (6)
14-12-14-2	40.47427305 (3)	71 (10)
13-12-14-5	43.18106187 (2)	73 (9)
13-12-14-1	60.83711083 (1)	92 (1)

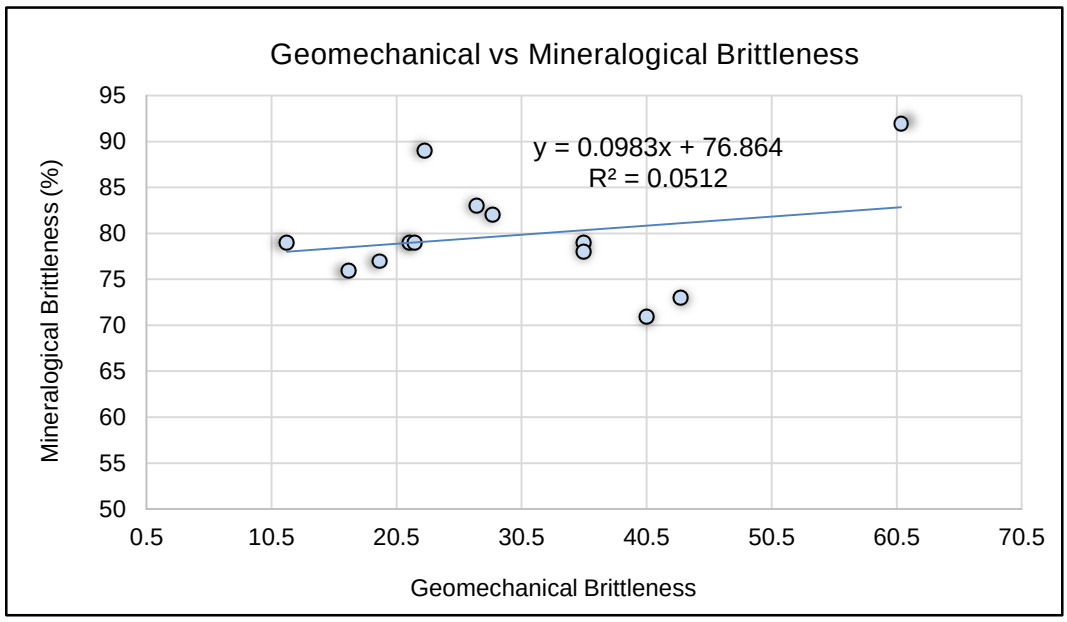

Figure 5-9. Correlation of the Geomechanical Brittleness versus the Mineralogical Brittleness – Del Rio, TX

Chapter 6

Conclusions

The results from Equation 14 should yield a linear best fit line with a positive slope if the samples from the area were subjected to the same strain state. If the data does not plot as a strain line, the samples were either subjected to different strains or were deformed beyond its tensile strength, or developed touching stress shadows limiting further joint development.

Palo Duro Canyon, TX showed signs of a positive correlation, yielding a positive slope from the Equation 14 plot. This suggests that the samples were subjected to the same strain state. The Bighorn Basin, WY samples did not yield a positive slope but considering the lack of sampling, a definitive strain state result cannot be established. In order to provide a definitive result for the study area, analysis of additional samples from the Bighorn Dolomite need to be collected along with the adjacent formations. Lastly, results indicate that the samples from Del Rio, TX were either subjected to different strain states or deformed beyond their tensile strength due to the negative slope and low correlation coefficient shown in Figure 5-7.

Considering the values of fracture toughness were estimated from multiple sources, future research would benefit from direct measurement. The fracture toughness of each rock varies significantly, resulting in a wide range of values to choose from. Analysis generally relies on estimations of rocks with similar composition rather than direct measurement. One specific instance would be Rijken and Cooke (2001), where the mean fracture toughness of the Austin Chalk was estimated from limestone in Birch (1966) and Atkinson and Meredith (1987). Zoback (2007) also indicates that “while fracture toughness is important for fracture initiation, once a fracture propagates past a

few tens of centimeters, extremely small pressures in excess of least principal stress are required to make the fracture grow, regardless of toughness".

Results from the Geomechanical Brittleness and Mineralogical Brittleness Index indicate that the two methods differ significantly, especially in the large data set from Del Rio. Because the Brittleness Index does not directly measure the mechanical properties of the rock but instead uses mineralogical content as a proxy, this could negatively impact the overall correlation. Porosity could also have an effect on the brittleness results. Because rock porosity affects mechanical properties, larger porosity may result in an overall decrease in rock brittleness (Heidari et al, 2013). Additionally, the pore structure within the samples could influence the acoustic velocities during testing (Winkler and Murphy, 1995). Winkler and Murphy (1995) go on to state that a lower porosity can have a greater effect if the porosity is contained in relatively thin, flat cracks. On the other hand, the same amount of porosity in spheroidal pores has a minimal effect on velocity.

As stated by Rickman et al (2008), "…each reservoir is unique and the stimulation and completion method should be determined based on its individual petrophysical attributes". Many of the other attempts to measure brittleness involve the use of Young's Modulus and Poisson's Ratio. As shown in Equation 13, those elastic components aren't the only factors effecting brittleness. The lack of a correlation of the geomechanical brittleness to the mineralogical brittleness may result from just that. A correlation of additional tests, such as an acid solubility test (AST) and capillary suction time test (CST), could also be compared to the geomechanical rock brittleness. Both AST and CST were utilized by Rickman et al. (2008) in a subsequent comparison with XRD.

Understanding the mechanics of fracture propagation is still an ongoing area of research within the oil and gas industry. Tiryaki (2006) goes as far as to state that “rock brittleness must be taken or considered as a rock behavior rather than an intrinsic rock property”. An improved understanding of rock brittleness may ultimately lead to a better modeling for hydraulic fracture stimulation.

References

Backers, T. (2005). Fracture toughness determination and micromechanics of rock under mode I and mode II loading. PhD thesis, University of Potsdam

Barthelemy, J.F., Guiton, M.E., and J-M Daniel, J.M. (2009). Estimates of Fracture Density and Uncertainties from Well Data. International Journal of Rock Mechanics and Mining Sciences 46, (3): 590-603.

Beaudoin, N., Leprêtre, R., Bellahsen, N., Lacombe, O., Amrouch, K., Callot, J. P., and Daniel, J. M. (2012). Structural and microstructural evolution of the Rattlesnake Mountain Anticline (Wyoming, USA): New insights into the Sevier and Laramide orogenic stress build-up in the Bighorn Basin. *Tectonophysics*, *576*, 20-45.

Berg, C.R. (2012). The Effect of Fracture and Borehole Orientation on Fracture Frequency and Density. RDS Dip Systems. The Woodlands, TX.

Bourne, S. J., and Willemse, E. J. (2001). Elastic stress control on the pattern of tensile fracturing around a small fault network at Nash Point, UK. *Journal of Structural Geology*, *23*(11), 1753-1770.

Brister, B. S., Stephens, W. C., and Norman, G. A. (2002). Structure, stratigraphy, and hydrocarbon system of a Pennsylvanian pull-apart basin in north-central Texas. *AAPG bulletin*, *86*(1), 1-20.

Chiles, J.P., Beucher, H., Wackernagel, H., Lantuejoul, C., and Elion, P. (2008). Estimating fracture density from a linear or aerial survey. Proceedings of the VIII International Geostatistics Congress, *ed.* J. Ortiz and X. Emery. V. 1, p. 535-544.

Diffendal, R. F. (1984). Comments on the geologic history of the Ogallala Formation in the southern panhandle of Nebraska. *Papers in Natural Resources*, 116.

Dutton, S. P., Finley, R.J., and Galloway, W.E. (1978). Geology and Geohydrology of the Palo Duro Basin, Texas Panhandle. Bureau of Economic Geology, University of Texas at Austin.

Dutton, S. P., Goldstein, A. G., and Ruppel, S. C. (1982). Petroleum potential of the Palo Duro Basin, Texas Panhandle. Bureau of Economic Geology, University of Texas at Austin.

Felzer, K. R., Abercrombie, R. E., and Brodsky, E. E. (2003, December). Testing the stress shadow hypothesis. In *AGU Fall Meeting Abstracts* (Vol. 1, p. 04).

Ferrill, D. A., McGinnis R. N., Morris, A.P., Smart, K.J., Sickmann, Z.T., Bentz, M., Lehrmann, D., and Evans, M.A. (2014). Control of mechanical stratigraphy on bed – restricted jointing and normal faulting: Eagle Ford Formation, south – central Texas. AAPG Bulletin 98, (11): 2477-2506.

Finn, T. M., Kirschbaum, M. A., Roberts, S. B., Condon, S. M., Roberts, L. N. R., and Johnson, R. C. (2010). Cretaceous–Tertiary Composite Total Petroleum System

(503402), Bighorn Basin, Wyoming and Montana. In *US Geological Survey Digital Data Series DDS–69–V* (p. 157).

Fox, J.E. and Dolton, G.L. (1996). Petroleum Geology of the Bighorn Basin, North-Central Wyoming and South-Central Montana. Resources of the Bighorn Basin; 47th Annual Field Conference Guidebook. WGA, 2005.

Gao, Z., and Hu, Q. (2013). Estimating permeability using median pore-throat radius obtained from mercury intrusion porosimetry. *Journal of Geophysics and Engineering*, *10*(2), 025014.

Hamlin, H. S. (2009). Ozona sandstone, Val Verde Basin, Texas: Synorogenic stratigraphy and depositional history in a Permian foredeep basin. *AAPG bulletin*, *93*(5), 573-594.

Handford, C. R., and Dutton, S. P. (1980). Pennsylvanian-Early Permian depositional systems and shelf-margin evolution, Palo Duro basin, Texas. *AAPG Bulletin*, *64*(1), 88-106.

Harris, R. A. (1998). Introduction to special section: Stress triggers, stress shadows, and implications for seismic hazard. *Journal of Geophysical Research: Solid Earth*, *103*(B10), 24347-24358.

Heidari, M., Khanlari, G. R., Torabi-Kaveh, M., Kargarian, S., and Saneie, S. (2014). Effect of porosity on rock brittleness. *Rock mechanics and rock engineering*, *47*(2), 785.

Hucka, V., and Das, B. (1974). Brittleness determination of rocks by different methods. In *International Journal of Rock Mechanics and Mining Sciences & Geomechanics Abstracts* (Vol. 11, No. 10, pp. 389-392). Pergamon.

Irwin, G. R. (1956). Onset of Fast Crack Propagation in High Strength Steel and Aluminum Alloys, Sagamore Research Conference Proceedings, Vol. 2, 289-305.

Keefer, W.R., Finn, T.M., Johnson, R.C., and Keighin, C.W., (1998). Regional stratigraphy and correlation of Cretaceous and Paleocene rocks, Bighorn Basin, Wyoming and Montana, *in* Keefer, W.R., and Goolsby, J.E., eds., Cretaceous and lower Tertiary rocks of the Bighorn Basin, Wyoming and Montana. Wyoming Geological Association 49th Guidebook, p. 1–30.

Lock, B. E., and Peschier, L. Boquillas (Eagle Ford) upper slope sediments, west Texas: Outcrop analogs for potential shale reservoirs. (2006): 491-508.

Lock, B. E., and Peschier, L., Fife, A., and Wawak, B. (2010). Boquillas (Eagle Ford) Formation and Associated Strata in Val Verde County, Texas. South Texas Geological Society Guidebook, p 1-84.

Mallman, E. P., and Parsons, T. (2008). A global search for stress shadows. *Journal of Geophysical Research: Solid Earth*, *113*(B12).

Mauldon, M., Dunne, W.M., and Rohrbaugh, M.B. (2001). Circular Scanlines and Circular Windows; New Tools for Characterizing the Geometry of Fracture Traces. Journal of Structural Geology 23, (2-3): 247-258.

Murry, P.A. (1989). Geology and Paleontology of the Dockum Formation (Upper Triassic), West Texas and Eastern New Mexico. Department of Physical Sciences, Tarleton State University, Stphenville.

Nagel, N., Zhang, F., Sanchez-Nagel, M., and Lee, B. (2013, May). Quantitative Evaluation of Completion Techniques on Influencing Shale Fracture 'Complexity'. In *ISRM International Conference for Effective and Sustainable Hydraulic Fracturing*. International Society for Rock Mechanics.

Nagel, N., Zhang, F., Sanchez-Nagel, M., Lee, B., and Agharazi, A. (2013, November). Stress shadow evaluations for completion design in unconventional plays. In *SPE Unconventional Resources Conference Canada*. Society of Petroleum Engineers.

Pearson, K. (2012). Geologic Models and Evaluation of Undiscovered Conventional and Continuous Oil and Gas Resources: Upper Cretaceous Austin Chalk, US Gulf Coast. US Department of the Interior, US Geological Survey.

Presley, M. W. (1987). Evolution of Permian Evaporite Basin in Texas Panhandle. *AAPG Bulletin*, *71*(2), 167-190.

Ren, L., Zhao, J., and Hu, Y. (2014). Hydraulic Fracture Extending into Network in Shale: Reviewing Influence Factors and Their Mechanism. The Scientific World Journal, vol. 2014, Article ID 847107, 9 pages, 2014. doi:10.1155/2014/847107

Rickman, R., Mullen, M. J., Petre, J. E., Grieser, W. V., and Kundert, D. (2008). A practical use of shale petrophysics for stimulation design optimization: All shale plays are not clones of the Barnett Shale. In *SPE Annual Technical Conference and Exhibition*. Society of Petroleum Engineers.

Rijken, P., and Cooke, M. L. (2001). Role of shale thickness on vertical connectivity of fractures: application of crack-bridging theory to the Austin Chalk, Texas. *Tectonophysics*, *337*(1), 117-133.

Rose, P.R. (1986). Hydrocarbon Resources of the Palo Duro Basin, Texas Panhandle. Office of Nuclear Waste Isolation, Technical Report.

Rose, P.R. (1986). Petroleum Geology of the Palo Duro Basin, Texas Panhandle. Office of Nuclear Waste Isolation, Technical Report.

Shi, G. C. (1985). Mechanics and Physics of Energy Density Theory. Theoretical and Applied Fracture Mechanics 4: 157-173

Singh, D. P., Sastry, V. R., and Srinivas, P. (1989). Effect of Strain Rate on Mechanical Behavior of Rocks. In *ISRM International Symposium*. International Society for Rock Mechanics.

Steidtmann, J.R., (1993). The Cretaceous foreland basin and its sedimentary record, in Snoke. Geology of Wyoming: Geological Survey of Wyoming Memoir, no. 5, p. 250–271.

Jin, Z. H., and Sun, C. T. (2005). Cohesive zone modeling of interface fracture in elastic bi-materials. *Engineering fracture mechanics*, *72*(12), 1805-1817.

Tapp, B., S., McGinty-Davis, L., Lortz and Schlagel, M. (1999). Fracture Architecture of the Tensleep Sandstone, Bighorn Basin, Wyoming; Surface Analogs for Subsurface Reservoirs. AAPG Bulletin 83, (7): 1189-1189.

Tan, Y., Johnston, T., and Engelder, T. (2014). The concept of joint saturation and its application. AAPG Bulletin, 98(11), 2347-2364.

Thomas, J., Koppenhoefer, K. C., and Crompton, J. S. (2014). Small Scale Yielding Model for Fracture Mechanics.

Tiryaki, B. (2006). Evaluation of the indirect measures of rock brittleness and fracture toughness in rock cutting. *JOURNAL-SOUTH AFRICAN INSTITUTE OF MINING AND METALLURGY*, *106*(6), 407.

Wang, F.P., and J. F. W. Gale, (2009). Screening Criteria for Shale-Gas Systems: GCAGS Transactions, 59, 779 - 793.

Ward, B., (2006). Geologic History of South Central Texas. Boerne Chapter, NPSOT.

Webb, P. A. (2001). An introduction to the physical characterization of materials by mercury intrusion porosimetry with emphasis on reduction and presentation of experimental data. *Micromeritics Instrument Corp, Norcross, Georgia*.

Wickham, J.S., Yu, X., and McMullen, R. (2013). Geomechanics of Fracture Density. Unconventional Resources Technology Conference, Paper 1619745

Winkler, K. W., and Murphy, W. F. (1995). Acoustic velocity and attenuation in porous rocks. *Rock physics & phase relations: a handbook of physical constants*, 20-34.

Wong, S.W., Geilikman, M., and Guanshui Xu, G. (2013). The Geomechanical Interaction of Multiple Hydraulic Fractures in Horizontal Wells, Effective and Sustainable Hydraulic Fracturing, Dr. Rob Jeffrey (Ed.), ISBN: 978-953-51-1137-5.

Willemse, E.J.M., D.C.P. Peacock, A. Aydin and D.O. Pollard. (1997). Relationship between Faults and Fractures in Tight Reservoirs. AAPG Bulletin 81: 1419-1420.

Wong, S. W., Geilikman, M., and Xu, G. (2013, May). The geomechanical interaction of multiple hydraulic fractures in horizontal Wells. In *ISRM International Conference for Effective and Sustainable Hydraulic Fracturing*. International Society for Rock Mechanics.

Wu, H. and D.D. Pollard. (1995). An Experimental Study of the Relationship between Joint Spacing and Layer Thickness. Journal of Structural Geology 17: 887-905

Zeeb, C., Gomez-Rivas, E., Bons, P.D., and Blum, P. (2013). Evaluation of sampling methods for fracture network characterization using outcrops. *AAPG Bulletin, 97*(9), 1545 – 1566.

Zastoupil, L. B. (2015). *A geomechanical equation for fracture density/brittleness and comparisons with a mineralogical brittleness index* (Doctoral dissertation, THE UNIVERSITY OF TEXAS AT ARLINGTON).

Zhang, Z. X., Kou, S. Q., Yu, J., Yu, Y., Jiang, L. G., and Lindqvist, P. A. (1999). Effects of loading rate on rock fracture. International Journal of Rock Mechanics and Mining Sciences, *36*(5), 597-611.

Zhixi, C., Mian, C., Yan, J., and Rongzun, H. (1997). Determination of Rock Fracture Toughness and its Relationship with Acoustic Velocity; Int. J. Rock Mech. And Min. Sci. 34: 3-4, Paper No. 49

Zoback, M. D. (2010). *Reservoir geomechanics*. Cambridge University Press.

Biographical Information

Derek Bammel received his Bachelors of Science in Geology from The University of Texas at Arlington in 2013. In fall of 2013, he entered the Graduate Program at The University of Texas at Arlington to pursue his studies in Petroleum Geology. Derek participated in the 2015 Imperial Barrel Awards, where the UTA team finished third place in the Southwest Section. His research interests revolve around Structural Geology, Geomechanics, and Planetary Science. After Graduation, Derek will continue working as a Business Analyst at Pioneer Natural Resources in Las Colinas, TX but will continue to seek out a Geologist position.